Surface & Coatings Technology 433 (2022) 128148

Contents lists available at ScienceDirect

Surface & Coatings Technology

journal homepage: www.elsevier.com/locate/surfcoat

Full length article

A zinc-doped coating prepared on the magnesium alloy by plasma electrolytic oxidation for corrosion protection

Chao Yang [a], Hu Cai [a], Suihan Cui [a,*], Jian Huang [a], Jiayu Zhu [a], Zhongcan Wu [a], Zhengyong Ma [a], Ricky K.Y. Fu [b], Liyuan Sheng [c], Xiubo Tian [a], Paul K. Chu [b], Zhongzhen Wu [a,*]

[a] School of Advanced Materials, Peking University Shenzhen Graduate School, Shenzhen 518055, China
[b] Department of Physics, Department of Materials Science & Engineering, and Department of Biomedical Engineering, City University of Hong Kong, Tat Chee Avenue, Kowloon 999077, Hong Kong, China
[c] PKU-HKUST ShenZhen-HongKong Institution, Shenzhen 518057, China

ARTICLE INFO

Keywords:
Magnesium alloy
Plasma electrolytic oxidation (PEO)
Zinc phosphate
Corrosion resistance

ABSTRACT

Corrosion protection of magnesium alloys is a challenge in industrial applications because of the high chemical reactivity of Mg. In this work, a coating is prepared by plasma electrolytic oxidation (PEO) on the AZ31B Mg alloy and then modified by insoluble zinc phosphate to improve the corrosion resistance. To avoid the influence of the weak acidic Zn-containing electrolyte on the formation of the passivation layer on the magnesium alloy, a two-step process is designed to first produce a passivation layer before introduction of zinc phosphate. Zinc phosphate is mainly distributed on the surface and the sidewalls of the holes in the porous coating and blocks the interactions between the corrosive solution and Mg substrate. The corrosion potential of the optimal coating (Zn-15) increase while the passive current density at the terminal potential decreases, suggesting the significantly improved corrosion resistance compared to the pristine AZ31B. The life time demonstrated by neutral salt spraying is 4200 h that is about 3 times longer than that observed from the Mg alloy with the undoped coating.

1. Introduction

Owing to the low density, high strength, and biodegradable properties, magnesium alloys are widely used in transportation, medical and other fields [1–3]. However, magnesium alloys are susceptible to corrosion because of the high chemical reactivity and severe corrosion and structural failure may result in the field [4–6]. Plasma electrolytic oxidation (PEO) is commonly used to generate a thick surface oxide layer in situ on valve metals to improve the corrosion resistance [7–10]. However, owing to the arc discharge, oxide coatings prepared by PEO contain many craters and holes which may become channels for external corrosive species to attack the substrate [7,11,12]. For example, the typical PEO coating prepared on the magnesium alloy surface can only survive for 300–500 h according to neutral salt spraying tests [13].

To improve the corrosion resistance, some inert organic substances such as epoxy resin, benzotriazole, and polytetrafluoroethylene have been employed to seal the holes [14–17], but the durability and mechanical properties can be compromised and in fact the lifetime can only be improved to 1000–1500 h [18,19]. Doping or modification of the PEO coatings with corrosion-resistant nanoparticles or insoluble compounds can increase the corrosion life [20–23]. We have demonstrated a long salt spraying lifetime of 11,000 h for aluminum alloys by introducing insoluble zinc phosphate (solubility product $K_{sp} = 9.1 \times 10^{-33}$) to the PEO coating resulting in a superhydrophilic surface with the self-healing capability to minimize corrosion through the holes [24]. However, compared to aluminum alloys, the Pilling-bedworth ratio of the oxide film (MgO) on magnesium alloys is smaller (<1) and therefore, acetate ions in the weak acidic Zn-containing electrolyte reduce the passivation effects and impede formation of the passivation layer [25,26]. Actually, an alkaline electrolyte can facilitate rapid passivation of magnesium alloys and produce continuous liquid plasma discharge [27,28], but precipitation can occur after additon of the Zn salt to reduce the stability of the PEO discharge.

In this work, an alkaline electrolyte is designed to create a passivation layer rapidly on the magnesium alloy in the stable PEO discharge until the passivation layer is robust enough. Afterwards, a weak acidic Zn-containing electrolyte is used to form the zinc phosphate modified PEO coating. Electrochemical and salt spraying assessment confirm the

* Corresponding authors.
E-mail addresses: cuish@pku.edu.cn (S. Cui), wuzz@pkusz.edu.cn (Z. Wu).

https://doi.org/10.1016/j.surfcoat.2022.128148
Received 4 December 2021; Received in revised form 17 January 2022; Accepted 19 January 2022
Available online 24 January 2022
0257-8972/© 2022 Published by Elsevier B.V.

uniform distribution of zinc phosphate on the surface as well as holes in the coatings, thereby impeding penetration of the external corrosive species and subsequent corrosion. A long lifetime of 4200 h is achieved as verified by the salt spraying test.

2. Material and methods

2.1. Materials

The magnesium alloy (AZ31B) was purchased from Dongguan Guanyue Metal Material Co., Ltd. (Dongguan, China) and cut into pieces with dimensions of 30 × 30 × 1 mm^3. Sodium hexametaphosphate ($(NaPO_3)_6$) was analytical grade and purchased from Aladdin Biochemical Technology Co., Ltd. (Shanghai, China). Analytical grade zinc acetate hydrate ($(CH_3COO)_2Zn{\cdot}xH_2O$) was obtained from Sinopharm Chemical Reagents Co., Ltd. (Shanghai, China). The other chemical reagents such as acetone, absolute ethanol, sodium hydroxide (NaOH), and sodium chloride (NaCl) were also analytical grade and bought from Guangdong Xilong Chemical Co., Ltd. (Shantou, China). The 1500 mesh metallographic sandpaper was obtained from 3M China Co., Ltd. (Shanghai, China). All the reagents were used without further purification.

2.2. Coating preparation

The AZ31B substrates were polished with 1500 mesh sandpaper and cleaned ultrasonically in deionized water, absolute ethanol, and acetone sequentially for 30 min. After drying, the coatings were prepared on the magnesium alloy samples by two-step PEO. Firstly, an alkaline electrolyte was used to prepare the passivated dielectric layer and then the sample was moved into another tank filling with a Zn-containing electrolyte to introduce zinc phosphate into the PEO coatings. In details, the alkaline electrolyte was prepared by mixing $(NaPO_3)_6$ (20 g), NaOH (3 g), and deionized water (1 L) and stirred at 400 r/min for 2 h until complete dissolution. The Zn-containing electrolyte contained 20 g of $NaPO_3$, 0/5/10/15 g of $(CH_3COO)_2Zn{\cdot}xH_2O$, and 1 L of deionized water. According to the Zn salt concentrations, the samples were designated as Zn-0, Zn-5, Zn-10, and Zn-15, respectively. The conductivity and the pH value of the different electrolyte was measured using a conductivity meter (DDS-307, Leici, China) and a pH meter (PHS-2F, Leici, China), respectively, as listed in Table S1. The sample and stainless steel container were the anode and cathode, respectively, and a 20 kW AC bipolar power supply (Plasma Technology Ltd., China) was operated in the constant current mode. The current density was 5.5 A/dm^2, frequency was 200 Hz, duty cycle was 12%, reaction time was 15 min (10 min for the alkaline electrolyte and 5 min for the Zn-containing electrolyte), and electrolyte temperature was below 40 °C.

2.3. Characterization

The morphology of the coatings was examined by field-emission scanning electron microscopy (FESEM, Carl Zeiss, SUPRA®55) and the chemical composition was determined by energy-dispersive X-ray spectroscopy (EDS, Oxford, X-Max20, England). X-ray diffraction (XRD, Bruker, D8 Advance) was performed to determine the crystal phases using a scanning rate of 5°/min and diffraction angles (2θ) from 10° to 80°. X-ray photoelectron spectroscopy (XPS, Thermo Fisher, ESCALAB 250×) was employed to determine the chemical composition and the spectra were referenced to the C1s peak (284.8 eV) and fitted with the Avantage 5.978 software. A focused ion beam instrument (FIB, Scios, FEI) was used to prepare the cross-sections prior to TEM examination. Transmission electron microscopy (TEM, JEM-3200FS, Japan) was carried out to characterize the structure and phase distribution in the coatings. The surface roughness was assessed on the surface roughness tester (JD220, JitaiKeyi, China) and the thickness was determined by an eddy current thickness meter (CTY2300, SDCH. Co., LTD). Five areas were analyzed to improve the statistics. The average aperture of the coating surface is measured by Nano Measurer software. 3D laser confocal scanning microscopy (LCSM, VK-X200 series, Keyence Corporation of America, USA) was performed to observe the contour of the coatings.

2.4. Corrosion resistance

The corrosion behavior of the coatings was evaluated by neutral salt spraying and electrochemical tests. The former was performed using a salt spraying instrument (SN-60A, Sannuo Instrument Co., Ltd., China) according to the ASTM B117 protocol. The concentration of NaCl was 5 wt%, the pH was 6.5–7.0, and the temperature was maintained at 35 °C. The electrochemical properties were studied by electrochemical impedance spectroscopy (EIS) and electrochemical curves (Tafel) were acquired on the workstation (NPROBE/EPC42, Zahner, Germany) at room temperature (25 °C). The experiments were performed in the 3.5 wt% NaCl solution based on the conventional three-electrode system, in which the platinum electrode, saturated calomel electrode (SCE) and sample with an exposed area of 2.4 cm^2 served as the counter electrode, reference electrode, and working electrode, respectively. The open circuit potential (OCP) was first monitored for 30 min to ensure equilibrium and then EIS was performed using a sinusoidal perturbation signal with an amplitude of 10 mV and frequencies from 100 kHz to 100 mHz. The results were fitted and analyzed by the ZsimpWin software. To ensure the reliability, the chi-square values (χ) of the impedance spectra was kept below 0.01 and the standard deviation was controlled to be within 10%. The Tafel data were collected at a scanning rate of 3 mV/s.

3. Results and discussion

Fig. 1 presents the voltage versus time curves of the magnesium alloy during PEO. In the constant current mode, the voltage increases gradually with time because of the increased resistance resulting from the formation of the insulating oxide. The discharge process can be divided into three stages. In the initial stage (0–180 s), the surface of the magnesium alloy is oxidized swiftly to generate a dense passivation film. Consequently, the reactive ions in the electrolyte accumulate on the passivation layer to increase the voltage. In the second stage (180–600 s), the discharge voltage (actual dynamic voltage) reaches the breakdown voltage of the insulating dielectric layer (when the coating starts to discharge) and breakdown occurs at the weak points to generate discharge channels and small dense electrical sparks. At this time, the molten metal from the high-temperature channels oxidizes rapidly and solidifies to produce the surface coating. As PEO proceeds, the electrical sparks become more intense giving rise to faster formation and larger

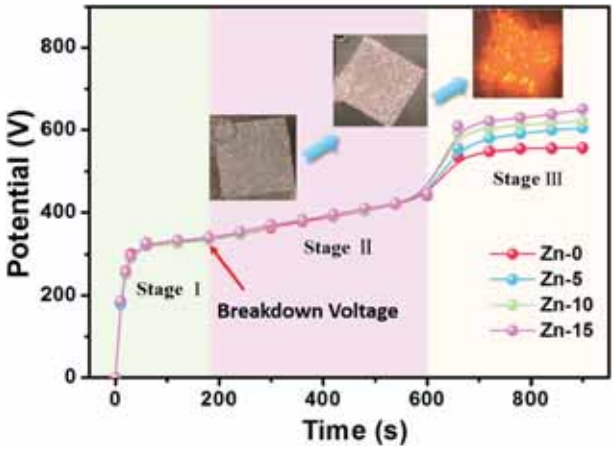

Fig. 1. The discharge voltage versus time curves obtained in the PEO experiments for different concentrations of Zn.

coating thickness. In the last stage (600–700 s), the alkaline electrolyte is replaced by the zinc-containing electrolyte, resulting in re-accumulation of charges on the coating surface. Therefore, the discharge voltage exhibits a sharp increase and the electrical sparks evolve into a bright yellow arc, which are different that observed from the conventional PEO process. After reaching the breakdown voltage again, the discharge voltage continues to increase with a lower speed. The voltage increases gradually as the zinc concentration in the electrolyte increases and the resistance of the PEO coating increases.

Fig. 2a shows the surface morphology of the PEO coatings with a crater-like porous structure showing molten bulges with different sizes distributed randomly on the surface, which is consistent with the morphology of passivation dielectric layer prepared by first step of PEO but the thickness is increase (Fig. S1). With increasing Zn concentration, the thickness increases from 33 ± 3 μm (Zn-0) to 58 ± 2 μm (Zn-15), indicating that the formation rate increases when the Zn salt is added to the electrolyte. Meanwhile, the larger thickness increases the intensity of individual sparks increasing the surface roughness Ra from 1.2 ± 0.2 μm (Zn-0) to 3.2 ± 0.3 μm (Zn-15), as shown in Figs. 2b and S2. However, the average size of the cracks and holes decreases gradually from 17.9 ± 5.5 μm (Zn-0) to 9.7 ± 4.8 μm (Zn-15) as shown in Fig. 2c, which may be attributed to backfill of Zn-containing compounds. The coatings are mainly composed of Mg, P, O, C and Zn according to EDS as shown in Fig. 2d, where C may derive from the organics exposed to air. With increasing Zn concentration in the electrolyte, the Zn concentration in the coating increases linearly reaching the maximum of 2.53 at.%. Fig. 2e displays the elemental maps of the cross-section and Zn exists primarily on the surface and side-walls of the holes.

The phase composition of the PEO coatings is determined by XRD as shown in Fig. 3a. All the diffraction peaks of metallic magnesium between 30° and 75° (PDF-#35-0821) are weaker from the PEO samples than the pristine AZ31B substrate. Only the typical $Mg_3(PO_4)_2$ (120) and MgO (111) diffraction peaks at 32.6° (PDF-#48-1167) and 36.9° are observed from Zn-0 (PDF-#45-0946) in addition to the Mg alloy peaks. With increasing Zn contents in the electrolyte, some new diffraction peaks appear at 22.1°, 27.5°, 30.6°, and 33.7° corresponding to the (101), (021), (121), and (130) planes of $Zn_3(PO_4)_2$ (PDF-#30-1490) suggesting the presence of $Zn_3(PO_4)_2$. A broad peak appears at 20°-35° when the Zn content is increased and it signifies an amorphous degree.

XPS (Fig. S3a) shows the similar coating composition (Mg, P, Zn, O, and C), where C may derive from the organics exposed to air. With increasing Zn contents, the characteristic peak of P 2p shifts to a higher

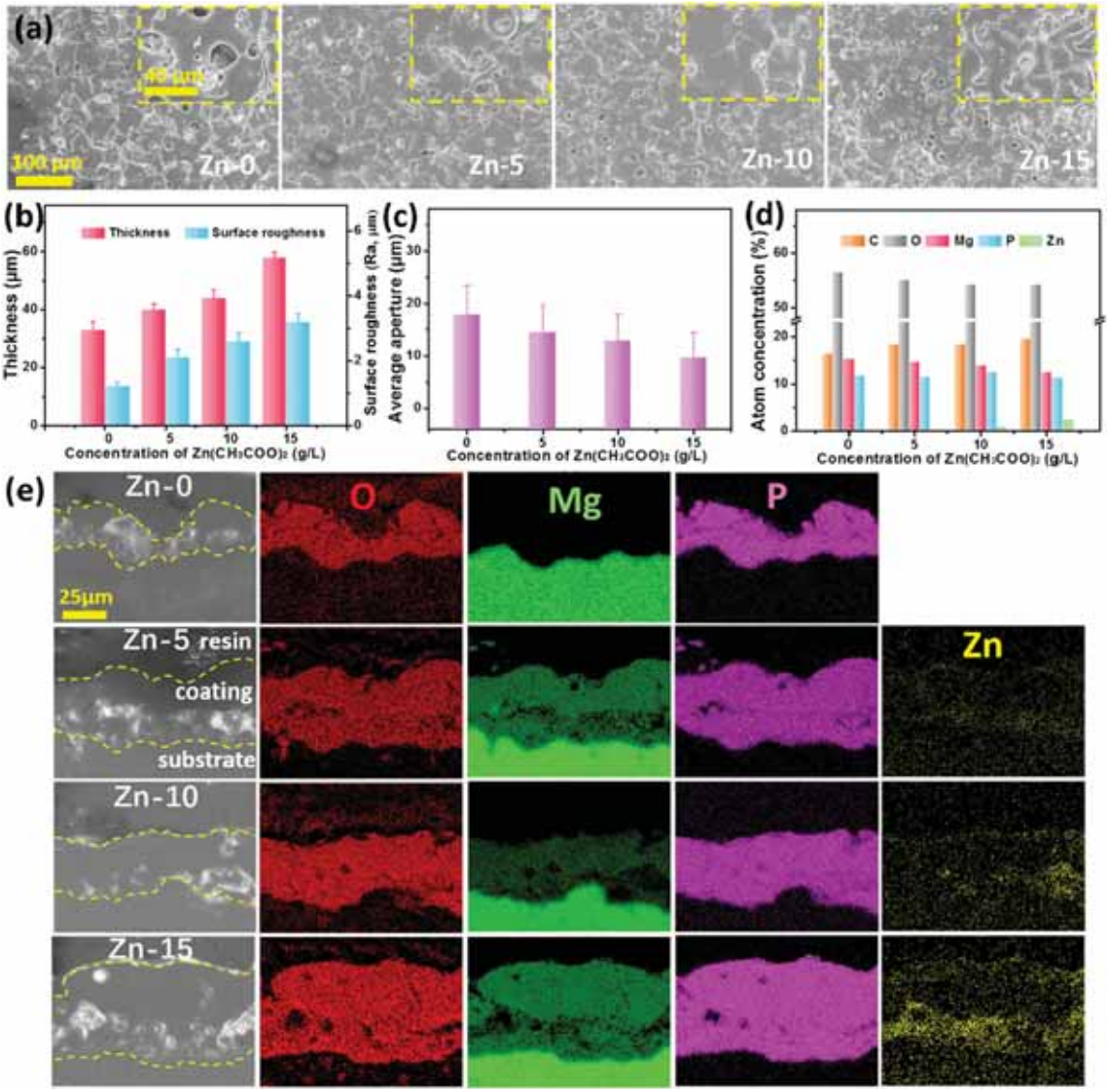

Fig. 2. Coatings prepared with different concentrations Zn: (a) SEM images; (b) Thickness and roughness; (c) Average pore size; (d) Elemental contents; (e) Cross-sectional morphology and elemental maps.

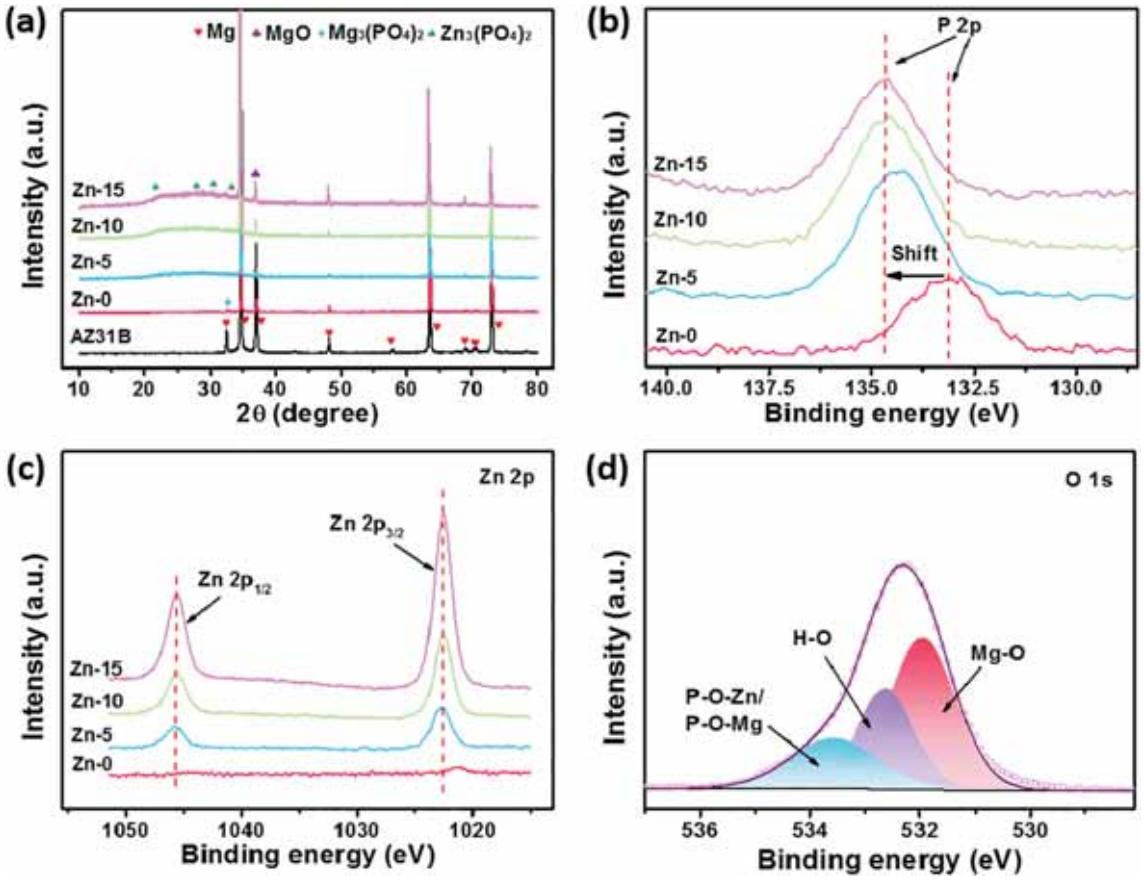

Fig. 3. Coatings prepared with different concentrations Zn: (a) XRD, (b) P 2p spectra of XPS, (c) Zn 2p spectra of XPS; (d) O 1s spectrum of Zn-15 of XPS.

binding energy, indicating the transition of the phosphate compounds in the surface of coatings, as shown in Fig. 3b [29]. Fig. 3c shows peaks of Zn $2p_{3/2}$ and Zn $2p_{1/2}$ at 1022.9 eV and 1044.8 eV, respectively, revealing that Zn is divalent [24,30]. The larger peak intensity indicates the increase of Zn concentration in the coating. The O1s peak of Zn-15 can be fitted into three sub-peaks with binding energies of 531.9 eV, 532.7 eV, and 533.6 eV, corresponding to Mg—O of MgO, H—O of hydroxide, and P—O—Zn and P—O—Mg of phosphate, respectively

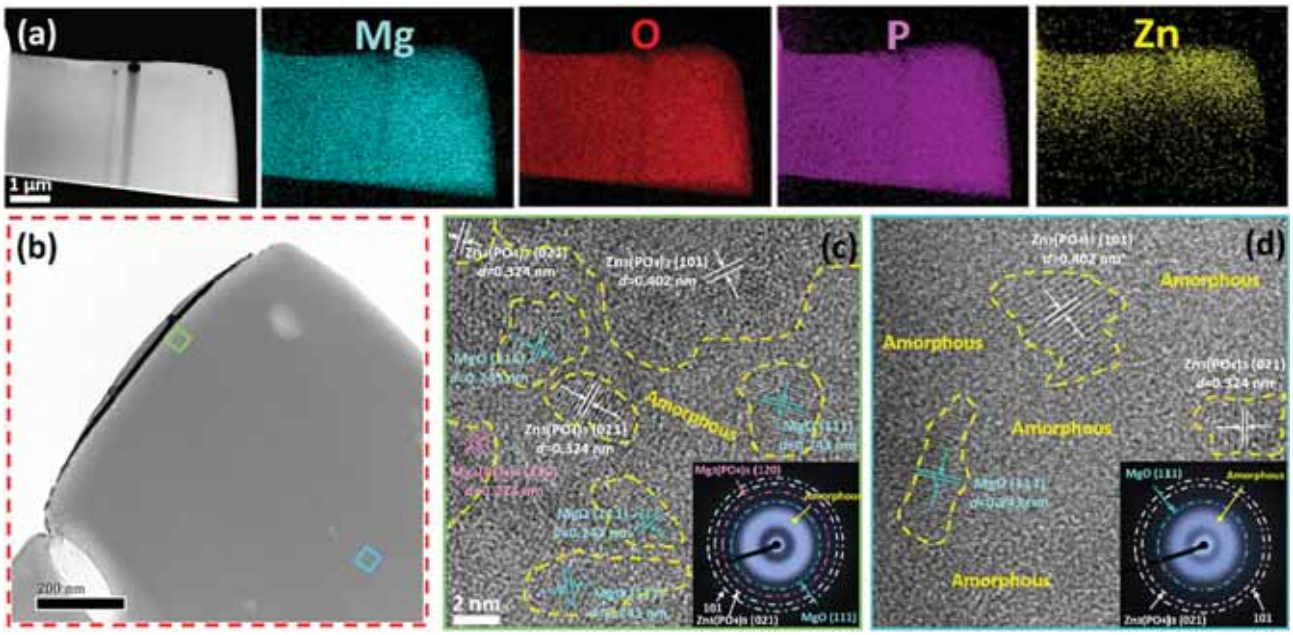

Fig. 4. TEM characterization results of Zn-15: (a) The cross-sectional elemental distributions and (b) Low-resolution TEM images, (c) High-resolution TEM image of the top region in the green box in (b), (d) High-resolution TEM image of the bottom region in the blue box in (b).

(Fig. 3d) [31–34]. Combined with the fitting peak of Mg 1s (Fig. S3b), the surface of Zn-15 coating consists of 71.12% of MgO, 24.24% of $Mg_3(PO_4)_2$ and 4.49% of $Zn_3(PO_4)_2$. For the coating prepared with different concentrations Zn, the contents of each component can be calculated from the cross-sectional EDS date (Fig. 2e), and the results are shown in Table S2. With increasing Zn salt concentration in the electrolyte, the amount of $Mg_3(PO_4)_2$ and $Zn_3(PO_4)_2$ increases but MgO decrease. This indicates that during the growth of the coating, some main phase MgO is replaced by the metal phosphide from the phosphate electrolyte.

Fig. 4 shows the TEM images of Zn-15 coating. Mg, O, and P are uniformly distributed in the coating but Zn mainly exists on the surface (Fig. 4a). Two regions (top and bottom of the coating marked in Fig. 4b) are selected and the high-resolution TEM images are depicted in Fig. 4c and d, respectively. Plenty of crystal grains with a grain size smaller than 10 nm are observed from the top surface. The d-spacings of the grains are 0.40 nm and 0.32 nm corresponding to the preferred orientations of $Zn_3(PO_4)_2$ (101) and (021), respectively, suggesting that Zn exists as $Zn_3(PO_4)_2$ in the coating. Some irregular nanocrystals of MgO (111), $Mg_3(PO_4)_2$ (120), and $Zn_3(PO_4)_2$ (021) are embedded in the amorphous MgO randomly below the top surface. In comparison, the proportion of the amorphous phase at the bottom of the coating is larger than that on the top surface. This may because that the arc energy increases gradually during coating formation, making more crystallization at the coating top surface.

The corrosion potentials (E_{corr}) and passive current densities (p_{corr}) at the terminal potential (p_{corr}) of the PEO coatings are obtained according to the Tafel curves shown in Fig. 5. The pristine AZ31B substrate shows the lowest corrosion potential (−1.462 V) and largest passive current density (2.050×10^{-3} A·cm^{-2}) (Table 1). Large amounts of black corrosion products appear from the AZ31B substrate, as shown by the optical images of the coatings after the dynamic potential test. In comparison, Zn-0 shows reduced corrosion as indicated by a larger corrosion potential of −1.230 V and smaller passive current density of 1.537×10^{-4}A·cm^{-2}. However, some obvious corrosion spots still exist on Zn-0. With increasing zinc phosphate concentration, the corrosion potential increases continuously, while the passive current density decreases. Consequently, with the exception of some corrosion spots, no obvious black corrosion products are observed from Zn-5 and Zn-10, and Zn-15 has the lowest electrochemical activity as manifested by the maximum corrosion potential of −0.938 V and minimum passive current density of 1.088×10^{-5} A·cm^{-2}.

Fig. 6 shows the optical images of the coatings with different Zn concentrations after neutral salt spraying. No significant corrosion spots

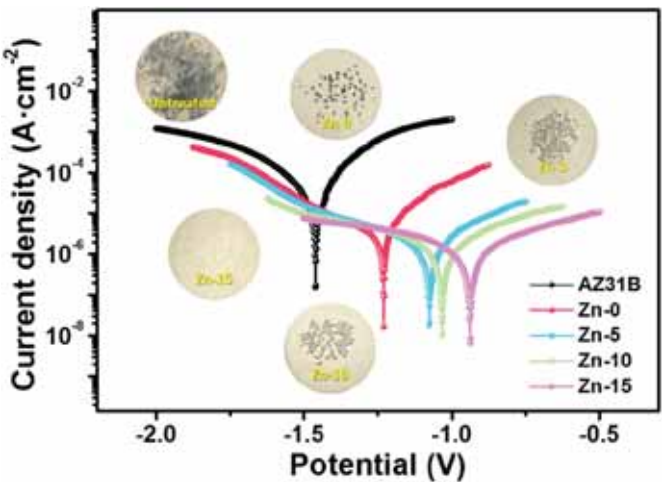

Fig. 5. Tafel curves of the AZ31B substrate and PEO coatings prepared with different concentrations of the Zn salt.

Table 1
Corrosion potentials, passive current densities at the terminal potential of different samples.

Samples	E_{corr} (V)	p_{corr} (A·cm^{-2})
AZ31B	−1.462	2.050×10^{-3}
Zn-0	−1.230	1.537×10^{-4}
Zn-5	−1.076	2.000×10^{-5}
Zn-10	−1.032	1.480×10^{-5}
Zn-15	−0.938	1.088×10^{-5}

appear from all the coatings in the first 600 h. After salt spraying for 1000 h, a visible corrosion spot is observed on Zn-0 but the modified zinc coatings are intact revealing positive protective effects rendered by Zn. With increasing corrosion time, the density and size of the corrosion spots on Zn-0 increase rapidly and some peeling occurs at the edge of the coating after 4200 h. In comparison, with increasing zinc phosphate concentrations, corrosion spots appear on Zn-5, Zn-10, and Zn-15 after 2000 h, 3000 h, and 4200 h, respectively. The service lifetime of Zn-15 is about 3 times that of Zn-0. The CLSM results (Fig. S4) are consistent with the optical images, revealing that the size and depth of the corrosion spots increase gradually during salt spraying.

EIS is performed to elucidate the corrosion mechanism after neutral salt spraying for different time. The Nyquist data, Bode impedance modulus, and Bode-phase angles are shown in Fig. 7 and the EIS data of AZ31B are shown in Fig. S5 and Table S3 for comparison. The untreated AZ31B substrate shows an obvious inductive arc [36] (Fig. S5), whereas the PEO coatings exhibit a capacitive behavior. The diameter of the capacitor arc increases with zinc phosphate concentration suggesting improved protection ability (Fig. 7a1, b1, c1, and d1). In the salt spraying process, the diameter of the capacitance arc declines rapidly indicative of worsening protection. The inductive arcs which indicate severe pitting appear from Zn-0, Zn-5, Zn-10, and Zn-15 after 1000 h, 2000 h, 3000 h, and 4200 h, respectively (Fig. 7b1, c1, and d1). According to the impedance modulus of the Bode-impedance at low frequency [37], the overall impedance of Zn-0 is 6.96×10^4 Ω·cm^2, which is more than 2 orders of magnitude larger than that of the AZ31B (1.84×10^2 Ω·cm^2), as shown in Fig. 7a2 and Fig. S5. The impedance increases further after modification with zinc phosphate and reaches a maximum of 2.78×10^5 Ω·cm^2 (Zn-15) and the coating resistance decreases gradually.

In the salt spraying process, inductance occurs at the low frequency segment in the Bode phase angle curves (Fig. 7a3, b3, c3, and d3), corresponding to the occurrence of pitting. The maximum position of the phase angles shifts with salt spraying time and the shift of Zn-0 and Zn-5 is larger than that of Zn-10 and Zn-15. This may be because active MgO (the main phase in Zn-0) has insufficient corrosion resistance in the long-term salt spraying test. Even though zinc phosphate improves the corrosion resistance of Zn-5, the porous structure provides ample corrosion sites. On the other hand, there is more zinc phosphate in Zn-10 and Zn-15 to cover the surface and holes to reduce contact between the active phase (such as MgO) and the corrosive medium. Besides, owing to the larger coating thickness and smaller holes, the corrosive electrolyte cannot penetrate to the substrate as easily and so that corrosion is impeded.

The EIS spectra are fitted with a complex nonlinear least squares method to investigate the corrosion behavior of the PEO coatings. Equivalent circuits (EC) with two or three time constants are obtained and the on-going physicochemical processes of the samples exposed to the corrosive environment are analyzed [38], as shown in Fig. 8. Generally, for PEO coating, the time constant corresponds to the layer numbers in the coating [22,39], so the EC can be determined according to the numbers of time constants in the Bode phase angles in Fig. 7. Actually, the coating prepared by the two-step method is different from the conventional PEO coating. The coating consists of the second step dense layer, the first step porous layer and the interface layer between

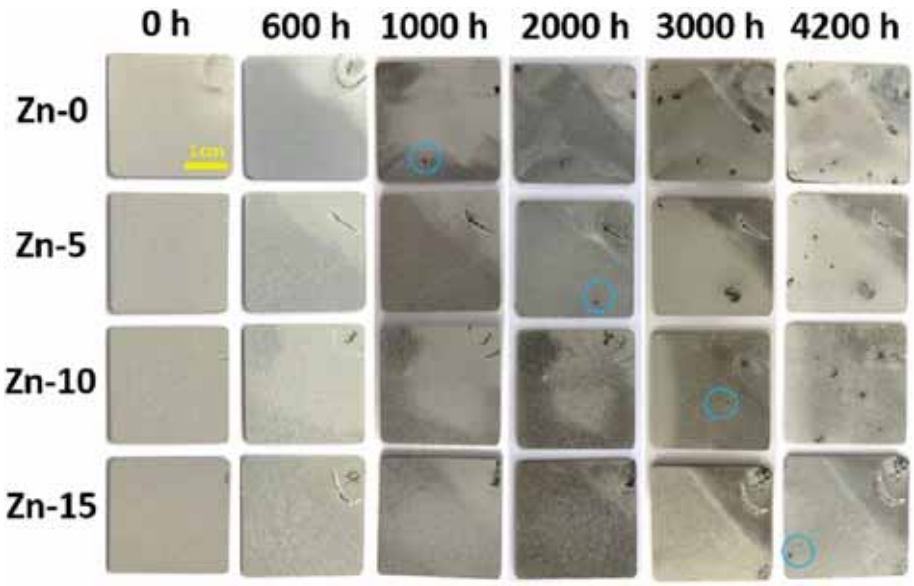

Fig. 6. Optical images of the PEO coatings with different Zn contents after neutral salt spraying.

the metal and the coating obtained by the two-step PEO, as shown in the cross-sectional SEM (Fig. 2e). The EIS of Zn-0 and Zn-15 show three time constants corresponding to aforementioned three layers, however, the Zn-5 and Zn-10 can only be fitted by two time constants corresponding to two layers. This may because that the second step layer and the first step layer are fused in the stable PEO process where has no obvious boundary between the upper layer and the middle layer (Fig. 2e). The time constant of the dense layer in Zn-0 disappears after salt spraying for 600 h, indicating commencement of corrosion (Fig. 7a3). However, the inductance does not appear suggesting that the corrosive medium has not penetrated into the interface between the substrate and coating at this time (Fig. 7a1). In comparison, the dense layer in Zn-15 disappears after 1000 h and inductance does not appear until 4200 h, thereby indicating better corrosion resistance and blocking ability.

Owing to the inhomogeneity caused by the chemical composition, crystallinity, stoichiometry, and space charge regions, it is difficult to analyze interfacial charge transfer by the ideal capacitors and resistors [40]. Therefore, some constant phase elements (*CPE*) are adopted to describe the non-ideal resistance and its impedance is mathematically given by Eq. (1):

$$Z_{CPE} = \frac{1}{T(j\omega)^n} \quad -1 \le n \le 1 \tag{1}$$

where T is the *CPE* coefficient, n is the *CPE* index, j is the complex unit of the imaginary number ($j=\sqrt{-1}$), and ω is the angular frequency (related to the frequency f (Hz), $\omega = 2\pi f$). The *CPE* is considered as an ideal capacitor, inductor, and resistor when n is equal to 1, −1 and 0, respectively. With regard to Zn-5 and Zn-10, the EIS spectra with and without pitting can be fitted with the ECs in Fig. 8a and c, respectively, where R_s is the solution resistance and CPE_p and R_p are the capacitance and porous layer resistance, respectively. CPE_{dl} and R_{ct} are the capacitance of the electrical double-layer and charge transfer resistance in the Faraday process, whereas L and R_l are the inductive and relative resistance caused by local corrosion. The capacitance and resistance of the inner dense layer are added to the ECs as shown in Fig. 8b and d.

Fig. 9 and Tables S4–S7 present the evolution of the electrical parameters (capacitance, resistance and inductance) in the ECs with salt spraying time. Generally, constant phase element- coefficient, *CPE-T*, cognates to the interfacial capacitance [41]. It is well known that capacitance is directly proportional to surface area and dielectric property and inversely proportional to the medium thickness of the charge separation. Therefore, for PEO coatings, its *CPE-T* value is mainly determined by the pore area, dielectric property, and coating thickness [42]. With increasing zinc phosphate contents, CPE_p and CPE_{dl} decrease gradually by nearly two orders of magnitude from 2.496×10^{-6} $\Omega^{-1}\cdot cm^{-2}\cdot s^n$ and 5.437×10^{-6} $\Omega^{-1}\cdot cm^{-2}\cdot s^n$ (Zn-0) to 9.267×10^{-8} $\Omega^{-1}\cdot cm^{-2}\cdot s^n$ and 7.456×10^{-8} $\Omega^{-1}\cdot cm^{-2}\cdot s^n$ (Zn-15), respectively. This can be attributed to the coating with higher-content zinc phosphate has a larger thickness resulting in a relatively reduced capacitance. In comparison, the dense layer CPE_d of Zn-0 and Zn-15 are 4.236×10^{-8} $\Omega^{-1}\cdot cm^{-2}\cdot s^n$ and 7.452×10^{-8} $\Omega^{-1}\cdot cm^{-2}\cdot s^n$, respectively, and much smaller than those of the porous layer. This phenomenon can be explained by the denser structure than the porous layer. Generally, the capacitance increases in salt spraying because newly generated corrosion products increase the surface area and Cl^- enhances the conductivity [42,43]. However, no significant changes occur in the coating capacitance at the beginning of corrosion (600 h). Only CPE_p of Zn-0 and Zn-5 shows a small reduction to 1.815×10^{-6} $\Omega^{-1}\cdot cm^{-2}\cdot s^n$ and 2.349×10^{-6} $\Omega^{-1}\cdot cm^{-2}\cdot s^n$, respectively, as shown in Fig. 9a. This is maybe because accumulation of corrosion products increases the specific surface area of the dielectric layer, but this effect is offset by the decrease in the dielectric constant [14]. In contrast, Zn-10 and Zn-15 which have high zinc phosphate concentrations prevent attack by the corrosive electrolyte in this stage. As corrosion continues, the specific surface area of the corrosion products increases, but the dielectric properties do not worsen giving rise to larger *CPE-T* value (Fig. 9a and c). Obviously, the *CPE-T* value of the Zn-doped coatings are smaller than that of the undoped coating.

In contrary to the *CPE-T* value, the porous layer resistance R_p and charge transfer resistance R_{ct} decrease during salt spraying as shown by Fig. 9b and d. Because of the holes in the porous layer, Cl^- can easily penetrate the coating longitudinally. The initial corrosion product Mg$(OH)_2$ dissolves readily to form water-soluble $MgCl_2$ when the pH of the electrolyte is below 10.5 resulting in smaller resistance [44,45]. After salt spraying for 4200 h, R_p and R_{ct} of Zn-0 decrease from 358.3 $\Omega\cdot cm^2$ and 3368 $\Omega\cdot cm^2$ to 29.9 $\Omega\cdot cm^2$ and 257 $\Omega\cdot cm^2$, respectively. With increasing zinc phosphate content, R_p and R_{ct} decrease more slowly. R_p and R_{ct} of Zn-15 decrease from 5.783×10^4 $\Omega\cdot cm^2$ and 3.788×10^5 $\Omega\cdot cm^2$ to 1.99×10^4 $\Omega\cdot cm^2$ and 2.54×10^4 $\Omega\cdot cm^2$, respectively, indicating that zinc phosphate mitigates the corrosion rate at the interface. In particular, the resistance declines gradually in the early stage of corrosion contrary to the *CPE-T* value (Fig. 9b and d). This is because accumulation of corrosion products on the surface or holes partially

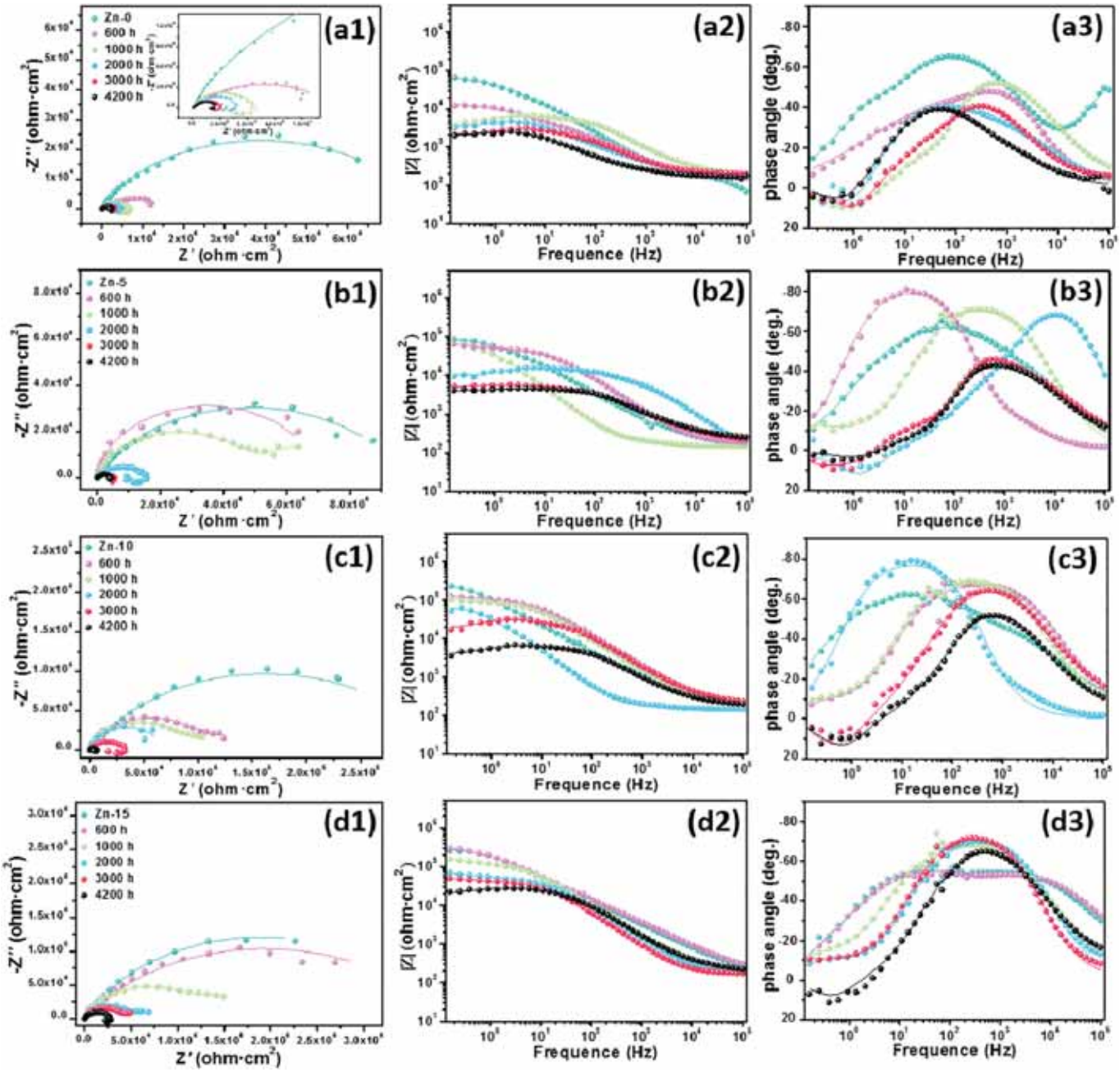

Fig. 7. EIS fitting curves for the PEO coatings after different salt spraying time with 5 wt% NaCl solution (Nyquist data and Bode data): (a1–a3) Zn-0, (b1–b3) Zn-5, (c1–c3) Zn-10, and (d1–d3) Zn-15.

blocks penetration of the corrosive electrolyte to the interface between the substrate and coatings through the dielectric layer and consequently reduces the ion paths towards the substrate.

Fig. 10 depicts the morphology of the PEO coatings with different zinc phosphate contents after salt spraying for 4200 h. Fig. 10a1 shows a large number of cracks on Zn-0. The enlarged images of the holes and surface (Fig. 10a2 and a3) show that the surface and walls around the holes become rough and are occupied by typical honeycomb corrosion products indicating severe corrosion on the coating. In comparison, the zinc-doped coatings show better corrosion resistance. Zn-5 shows no obvious cracks and some areas retain the smooth morphology. The honeycomb corrosion products decrease obviously and only some corrosion products are observed from the holes and surface (Fig. 10b). With increasing zinc phosphate concentrations, the corrosion products decrease and the proportion of the un-corroded area increases (Fig. 10c and d). There is almost no honeycomb structure except a few micro corrosion products on Zn-15 (Fig. 10d). Fig. S6 displays the corrosion morphology of the PEO coatings with different Zn contents after salt spraying for different time. Zn-0 shows significant destruction after salt spraying for 600 h and some dense and sheet corrosion products are present on Zn-5. On the other hand, both Zn-10 and Zn-15 show no significant changes on the surface and around the holes.

To further analyze the reactions and corrosion products, XPS is performed after salt spraying for 4200 h. Fig.11a reveals both $Mg(OH)_2$ and $MgCl_2$ as indicated by the Mg 2p peak of Zn-0 and Zn-15 [46]. Hence, the corrosion reaction occurs on the main phase (MgO) in the coatings according to Eqs. (2) and (3):

$$MgO + H_2O \rightarrow Mg(OH)_2 \quad (2)$$

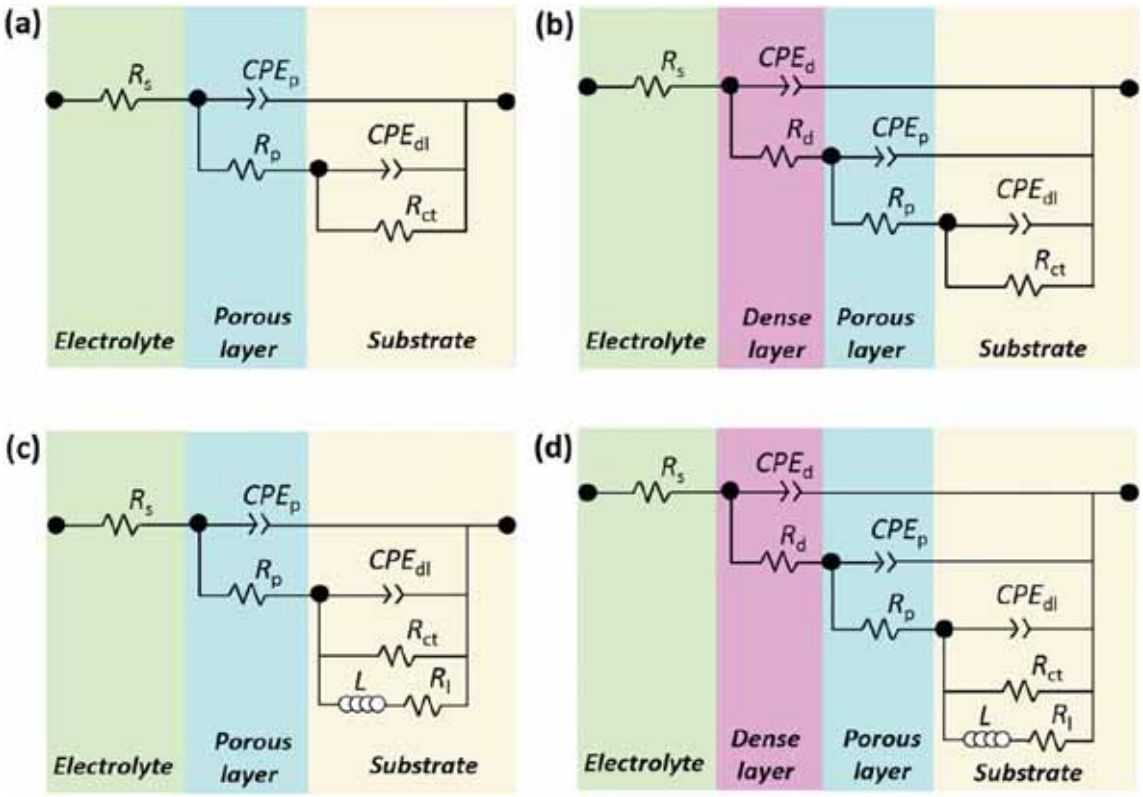

Fig. 8. Equivalent circuits based on the EIS data shown in Fig. 7: (a) Zn-5 and Zn-10 before corrosion, (b) Zn-0 and Zn-15 before corrosion, (c) Zn-5 and Zn-10 after corrosion, and (d) Zn-0 and Zn-15 after corrosion.

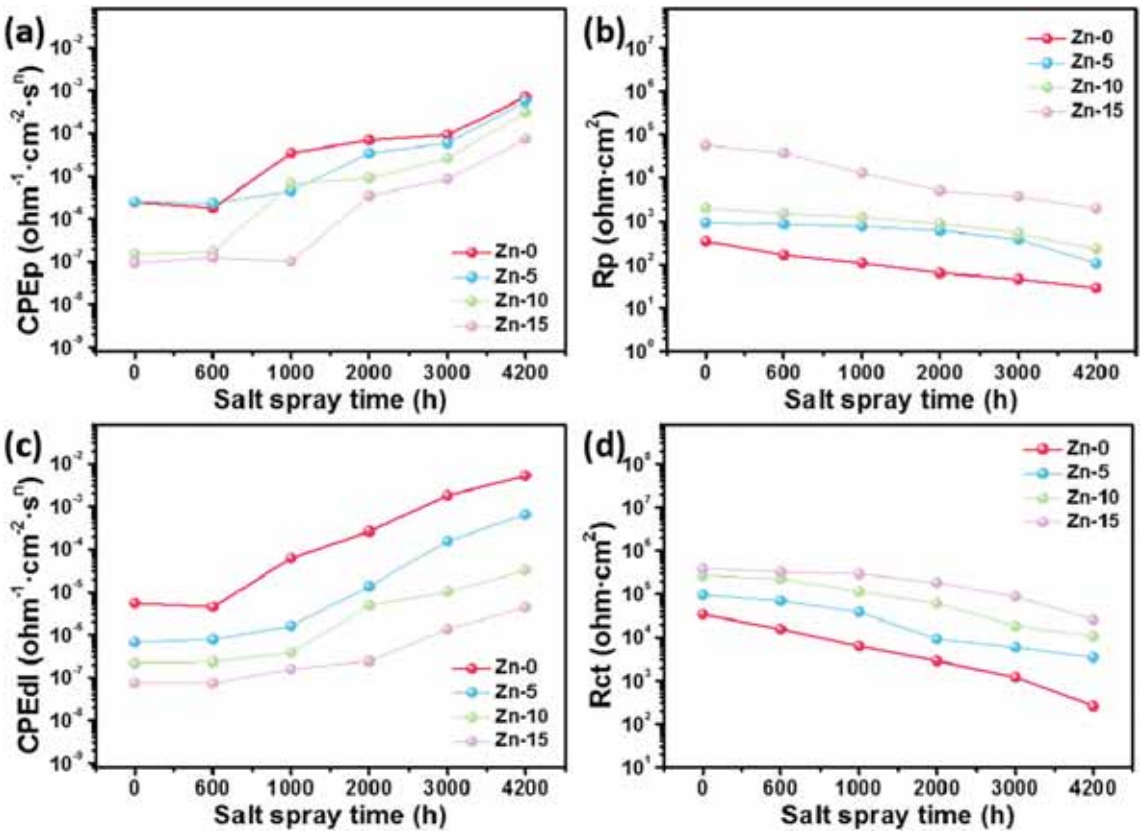

Fig. 9. Variations of the electrical parameters in the equivalent circuits: (a) CPE_p, (b) R_p, (c) CPE_{dl}, and (d) R_{ct}.

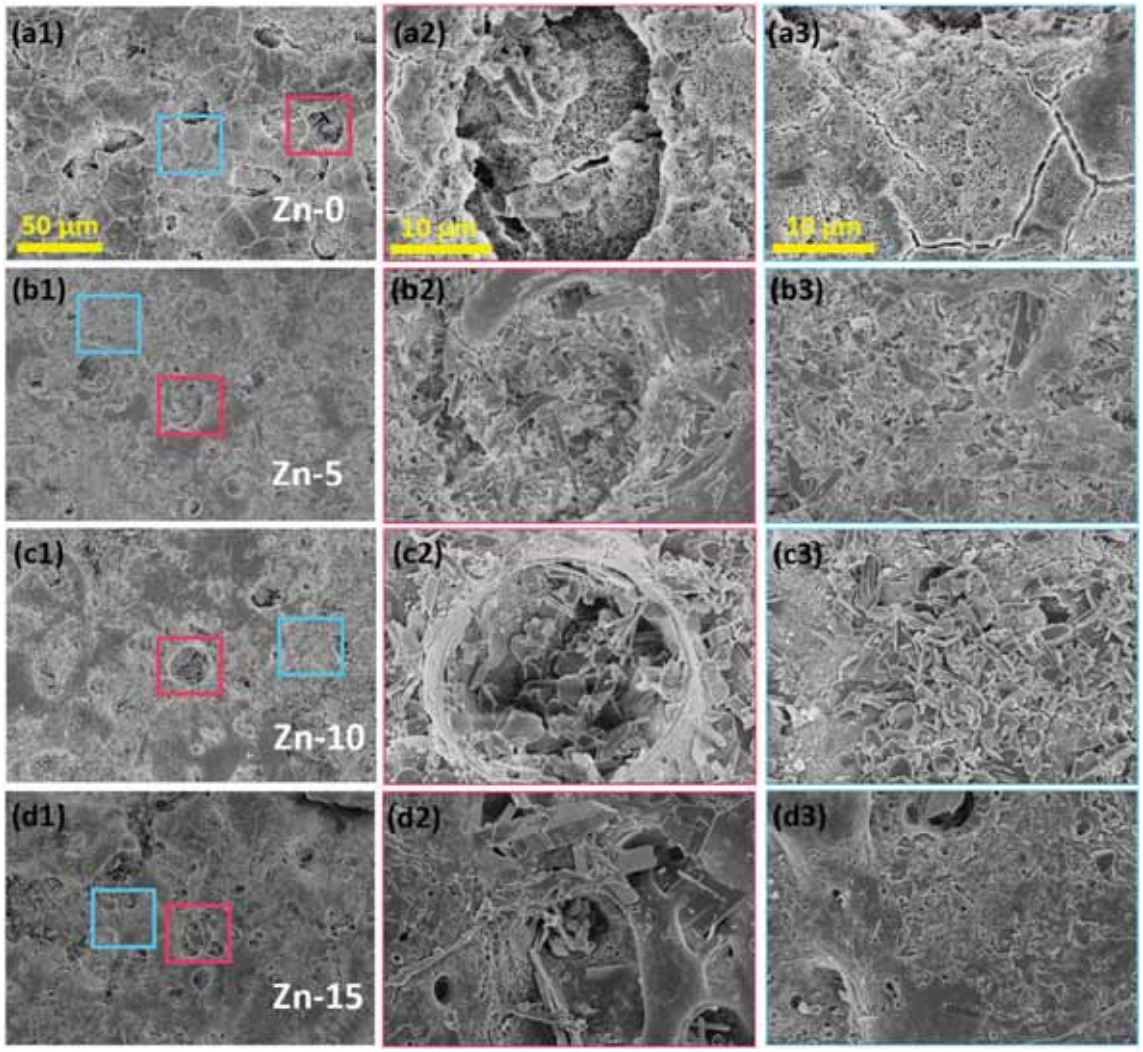

Fig. 10. SEM image of the coatings prepared with different concentrations of Zn salt after salt spraying for 4200 h: (a1–a3) Zn-0, (b1–b3) Zn-5, (c1–c3) Zn-10, and (d1–d3) Zn-15.

$$Mg(OH)_2 + 2Cl^- \rightarrow MgCl_2 + 2OH^- . \quad (3)$$

MgO is easily converted into $Mg(OH)_2$ with water and $Mg(OH)_2$ is soluble below a pH of 10.5. They can be converted into water-soluble $MgCl_2$ after absorption of Cl^- [47]. Compared to Zn-0, the peak areas of $Mg(OH)_2$ and $MgCl_2$ of Zn-15 sample are smaller, indicating that zinc phosphate impedes the corrosion reactions and reduces the corrosion rate.

Fig. 11b shows the O 1s spectra of Zn-0 and Zn-15. Different from Zn-0, $Zn_3(PO_4)_2$ and $Zn(OH)_2$ [30,48] are observed from Zn-15, revealing that $Zn_3(PO_4)_2$ participates in the corrosion reaction as shown in Eq. (4):

$$Zn_3(PO_4)_2 + 6OH^- \rightarrow 3Zn(OH)_2 + 2\,PO_4^{3-} \quad (4)$$

$Zn_3(PO_4)_2$ on the surface also dissolves in the long-term salt spraying test and reacts with OH^- to form the $Zn(OH)_2$. However, owing to the small solubility of $Zn_3(PO_4)_2$ [49], the corrosion rate is quite slow resulting in an effective protection. Similar to the protection on aluminum alloys [24], these PEO coatings on magnesium have porous and rough characteristics as well as superhydrophilicity (Fig. S7). The Zn-containing compound dissolved in the corrosive electrolyte migrate to nearby holes under the wetting force because of the super-hydrophilicity and is deposited around the holes to enhance the blocking effect of the corrosive electrolyte [24]. This represents a self-healing mechanism for a certain period of time (Figs. S8 and S9).

The corrosion resistance mechanism of the PEO coatings is shown in Fig. 12. With regard to the undoped coatings (Fig. 12a), the main constituent is MgO which could be easily converted into $Mg(OH)_2$ during salt spraying. Hence, the corrosive electrolyte penetrates longitudinally through weak holes in the outer layer to increase the specific surface area and enhance corrosion. Eventually, the electrolyte reaches the interface between the substrate and coating to produce large-area pitting and cracks. However, as for the zinc phosphate modified coatings (Fig. 12b), the zinc phosphate is mainly distributed on the surface and sidewalls of the holes and so direct contact between MgO and the corrosive medium is blocked. The inert zinc phosphate acts as a physicochemical barrier to reduce the corrosion rate. During salt spraying, zinc phosphate on the top surface reacts with the corrosive medium to form $Zn(OH)_2$ at a slow rate and so the paths to the substrate are blocked and the corrosion rate decreases.

4. Conclusion

A two-step PEO process is designed to produce coatings doped with zinc phosphate on the magnesium alloy and the corrosion resistance and underlying mechanism are investigated systematically. Zinc phosphate is present on the surface and sidewalls of the holes to block the reactions between the corrosive electrolyte and Mg active substrate. Electrochemical assessment reveals that the corrosion potential of the coating

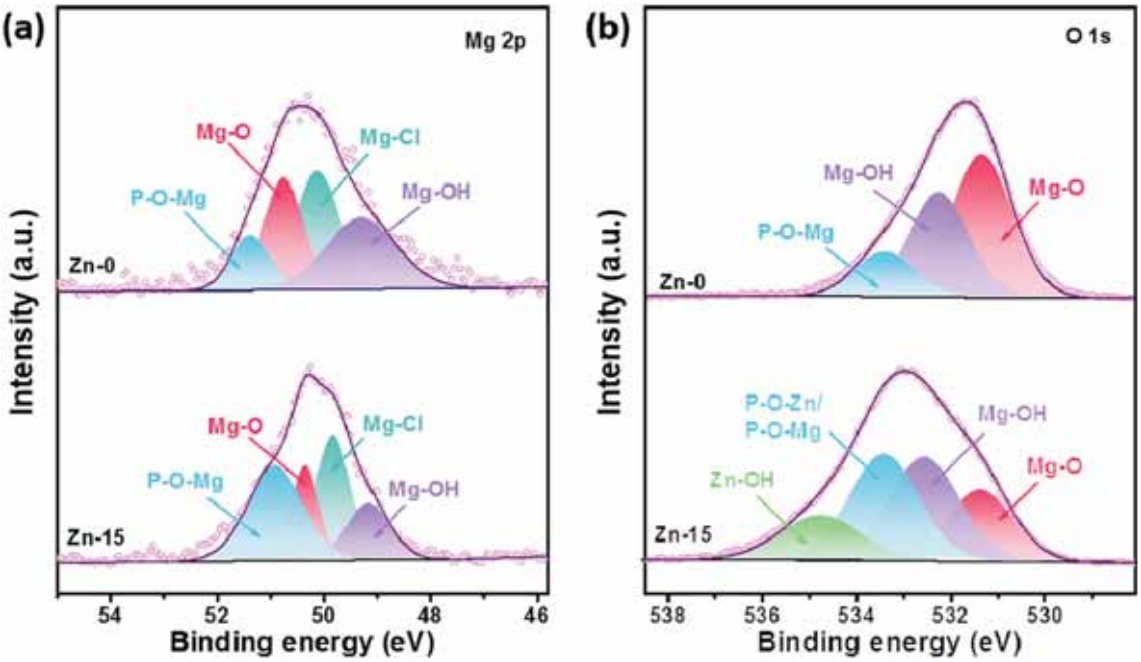

Fig. 11. XPS spectra of Zn-0 and Zn-15 after salt spraying for 4200 h: (a) Mg 2p peak and (b) O 1s peak.

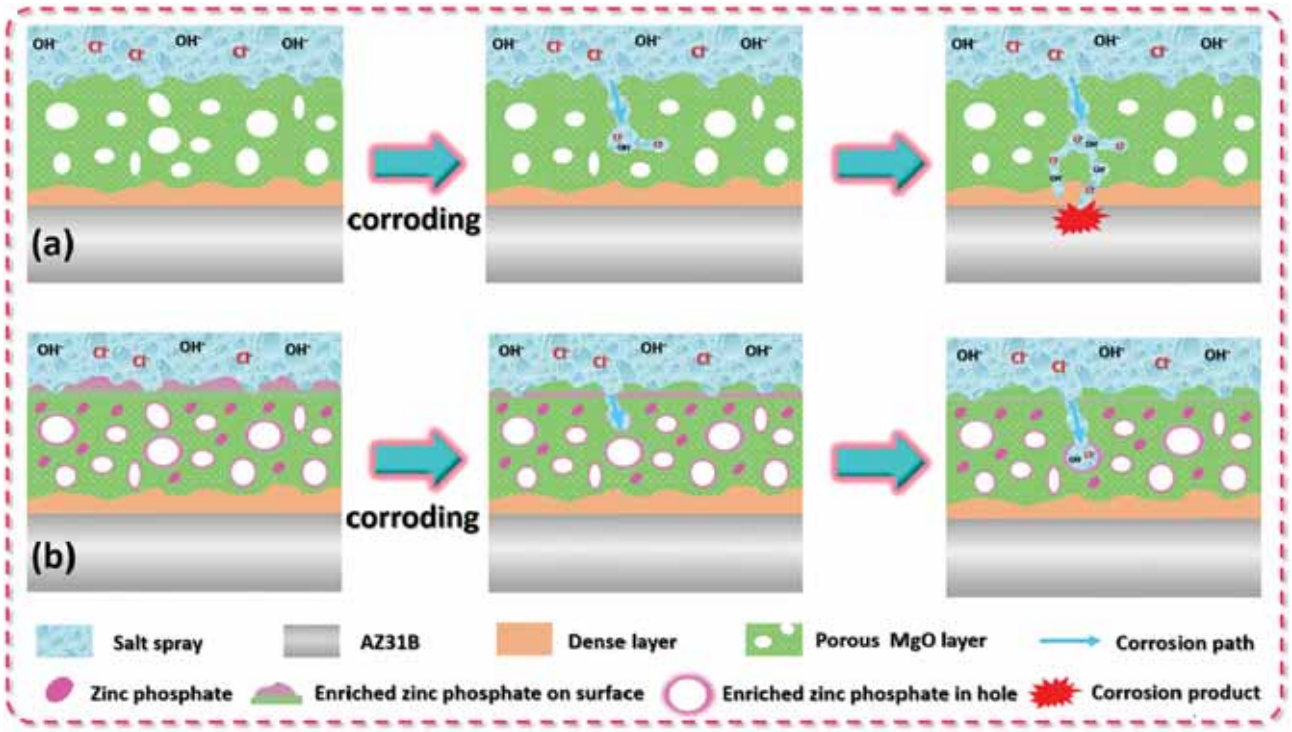

Fig. 12. Corrosion resistance mechanism of the PEO coatings produced on the magnesium alloy: (a) Mg substrate with PEO coating without zinc phosphate, (b) Mg substrate with the zinc phosphate PEO coating.

increases gradually but the passive current density at the terminal potential decreases with increasing Zn concentrations. EIS performed after salt spraying for different time discloses that zinc phosphate increases the porous layer resistance (R_p) and interface charge transfer resistance (R_{ct}) and impedes penetration and corrosion by the electrolyte. Consequently, the main phase of MgO is protected and the lifetime of the PEO coating is demonstrated to be 4200 h by the neutral salt spraying test.

CRediT authorship contribution statement

Chao Yang, Suihan Cui and Zhongzhen Wu proposed the research; Hu Cai, Jian Huang and Jiayu Zhu designed the coating depositions; Chao Yang, Zhongcan Wu and Zhengyong Ma did the coating characterizations and properties testing; Chao Yang, Ricky K. Y. Fu, Liyuan Sheng, Xiubo Tian, Paul K. Chu and Zhongzhen Wu analyzed and discussed the data; Chao Yang, Zhongzhen Wu wrote the paper; Suihan Cui,

Zhongzhen Wu and Paul K. Chu polished the English writing; all authors provided feedback.

Declaration of competing interest

The authors declare no competing financial interest.

Acknowledgements

This work was financially supported by the National Materials Genome Project (No. 2016YFB0700600), Peking University Shenzhen Graduate School Research Start-up Fund of Introducing Talent (No. 1270110273), Shenzhen Science and Technology Research Grants (JSGG20191129112631389), City University of Hong Kong Strategic Research Grant (SRG) No. 7005505 and IER Foundation (IERF2020001 and IERF2019002).

Appendix A. Supplementary data

Supplementary data to this article can be found online at https://doi.org/10.1016/j.surfcoat.2022.128148.

References

[1] W.Q. Xu, N. Birbilis, G. Sha, Y. Wang, J.E. Daniels, Y. Xiao, M. Ferry, A high specific-strength and corrosion-resistant magnesium alloy, Nat. Mater. 14 (2015) 1229–1235.
[2] S.V. Lamaka, B. Vaghefinazari, D. Mei, R.P. Petrauskas, D. Hoche, M. L. Zheludkevich, Comprehensive screening of mg corrosion inhibitors, Corros. Sci. 128 (2017) 224–240.
[3] J.F. Song, J. She, D.L. Chen, F.S. Pan, Latest research advances on magnesium and magnesium alloys worldwide, J. Magnes. Alloy 8 (2020) 1–41.
[4] X.G. Li, D.W. Zhang, Z.Y. Liu, Z. Li, C.W. Du, C.F. Dong, Materials science: share corrosion data, Nat. News 527 (2015) 441.
[5] Y. Wang, B. Liu, X.A. Zhao, X. Zhang, Y. Miao, N. Yang, B. Yang, L. Zhang, W. Kuang, J. Li, E. Ma, Z. Shan, Turning a native or corroded Mg alloy surface into an anti-corrosion coating in excited CO2, Nat. Commun. 9 (2018) 4058.
[6] X.J. Wang, D.K. Xu, R.Z. Wu, X.B. Chen, Q.M. Peng, L. Jin, Y.C. Xin, Z.Q. Zhang, Y. Liu, X.H. Chen, G. Chen, K.K. Deng, H.Y. Wang, What is going on in magnesium alloys? J. Mater. Sci. Technol. 34 (2018) 245–247.
[7] S.Q. Liu, Z.X. Li, Q.L. Yu, Y.M. Qi, Z.J. Peng, J. Liang, Dual self-healing composite coating on magnesium alloys for corrosion protection, Chem. Eng. J. 424 (2021), 130551.
[8] A.B. Khiabani, B. Yarmand, M. Mozafari, Enhanced corrosion resistance and in-vitro biodegradation of plasma electrolytic oxidation coatings prepared on AZ91 mg alloy using ZnO nanoparticles-incorporated electrolyte, Surf. Coat. Technol. 360 (2019) 153–171.
[9] J.F. Chen, W.X. Lin, S.Y. Liang, L.C. Zou, C. Wang, B.S. Wang, M.F. Yan, X.P. Cui, Effect of alloy cations on corrosion resistance of LDH/MAO coating on magnesium alloy, Appl. Surf. Sci. 463 (2019) 535–544.
[10] M. Toorani, M. Aliofkhazraei, M. Golabadi, A.S. Rouhaghdam, Effect of lanthanum nitrate on the microstructure and electrochemical behavior of PEO coatings on AZ31 mg alloy, J. Alloys Compd. 719 (2017) 242–255.
[11] G. Zhang, L. Wu, A.T. Tang, Y.L. Ma, G.L. Song, D.J. Zheng, B. Jiang, A. Atrens, F. S. Pan, Active corrosion protection by a smart coating based on a MgAl-layered double hydroxide on a cerium-modified plasma electrolytic oxidation coating on mg alloy AZ31, Corros. Sci. 139 (2018) 370–382.
[12] J.M. Zhao, X. Xie, C. Zhang, Effect of the graphene oxide additive on the corrosion resistance of the plasma electrolytic oxidation coating of the AZ31 magnesium alloy, Corros. Sci. 114 (2016) 146–155.
[13] D. Veys-Renaux, C.E. Barchiche, E. Rocca, Corrosion behavior of AZ91 mg alloy anodized by low-energy micro-arc oxidation: effect of aluminates and silicates, Surf. Coat. Technol. 251 (2014) 232–238.
[14] M. Toorani, M. Aliofkhazraei, M. Mahdavian, R. Naderi, Effective PEO/Silane pretreatment of epoxy coating applied on AZ31B mg alloy for corrosion protection, Corros. Sci. 169 (2020), 108608.
[15] D. Jiang, X.C. Xia, J. Hou, G.Y. Cai, X.X. Zhang, Z.H. Dong, A novel coating system with self-reparable slippery surface and active corrosion inhibition for reliable protection of mg alloy, Chem. Eng. J. 373 (2019) 285–297.
[16] M. Sun, A. Yerokhin, M.Y. Bychkova, D.V. Shtansky, E.A. Levashov, A. Matthews, Self-healing plasma electrolytic oxidation coatings doped with benzotriazole loaded halloysite nanotubes on AM50 magnesium alloy, Corros. Sci. 111 (2016) 753–769.
[17] A. Alabbasi, A. Mehjabeen, M.B. Kannan, Q.S. Ye, C. Blawert, Biodegradable polymer for sealing porous PEO layer on pure magnesium: an in vitro degradation study, Appl. Surf. Sci. 301 (2014) 463–467.
[18] Y.W. Song, K.H. Dong, D.Y. Shan, E.H. Han, Investigation of a novel self-sealing pore micro-arc oxidation film on AM60 magnesium alloy, J. Magnes. Alloy 1 (2013) 82–87.
[19] C. Liu, X.P. Lu, Y. Li, Q.Q. Chen, T. Zhang, F.H. Wang, Influence of post-treatment process on corrosion and wear properties of PEO coatings on AM50 mg alloy, J. Alloys Compd. 870 (2021), 159462.
[20] Z.U. Rehman, D.J. Choi, Investigation of ZrO2 nanoparticles concentration and processing time effect on the localized PEO coatings formed on AZ91 alloy, J. Magnes. Alloy 7 (2019) 555–565.
[21] X.J. Cui, C.H. Liu, R.S. Yang, Q.S. Fu, X.Z. Lin, M. Gong, Duplex-layered manganese phosphate conversion coating on AZ31 mg alloy and its initial formation mechanism, Corros. Sci. 76 (2013) 474–485.
[22] T.S. Lim, H.S. Ryu, S.H. Hong, Electrochemical corrosion properties of CeO2-containing coatings on AZ31 magnesium alloys prepared by plasma electrolytic oxidation, Corros. Sci. 62 (2012) 104–111.
[23] D.D. Zhang, F. Peng, X.Y. Liu, Protection of magnesium alloys: from physical barrier coating to smart self-healing coating, J. Alloys Compd. 853 (2021), 157010.
[24] Q. Huang, L.L. Liu, Z.Z. Wu, S. Ji, H. Wu, P.H. Chen, Z.Y. Ma, Z.C. Wu, R.K.Y. Fu, H. Lin, X.B. Tian, F. Pan, P.K. Chu, Corrosion-resistant plasma electrolytic oxidation coating modified by zinc phosphate and self-healing mechanism in the salt-spray environment, Surf. Coat. Technol. 384 (2020), 125321.
[25] J. Gray, B. Luan, Protective coatings on magnesium and its alloys-a critical review [J], J. Alloys Compd. 336 (2002) 88–113.
[26] R.F. Zhang, Film formation in the second step of micro-arc oxidation on magnesium alloys[J], Corros. Sci. 52 (2010) 1285–1290.
[27] Y.G. Ko, S. Namgung, D.H. Shin, Correlation between KOH concentration and surface properties of AZ91 magnesium alloy coated by plasma electrolytic oxidation, Surf. Coat. Technol. 205 (2010) 2525–2531.
[28] M.S. Jon, A. Fattah-alhosseini, Effect of KOH concentration on the electrochemical behavior of coatings formed by pulsed DC micro-arc oxidation (MAO) on AZ31B mg alloy, J. Alloys Compd. 661 (2016) 237–244.
[29] S.P. Ji, Y.C. Weng, Z.Z. Wu, Z.Y. Ma, X.B. Tian, R.K.Y. Fu, L. Hai, G.S. Wu, P.K. Chu, P. Feng, Excellent corrosion resistance of P and fe modified micro-arc oxidation coating on Al alloy, J. Alloys Compd. 710 (2017) 452–459.
[30] F. Jamali-Sheini, K.R. Patil, Synthesis of cu-ZnO and C-ZnO nanoneedle arrays on zinc foil by low temperature oxidation route: effect of buffer layers on growth, optical and field emission properties, Appl. Surf. Sci. 257 (2011) 8366–8372.
[31] N.V. Phuong, M. Gupta, S. Moon, Enhanced corrosion performance of magnesium phosphate conversion coating on AZ31 magnesium alloy, Trans. Nonferrous Metals Soc. China 27 (2017) 1087–1095.
[32] L. Pezzato, R. Babbolin, P. Cerchier, M. Marigo, P. Dolcet, M. Dabalà, Katya brunelli, sealing of PEO coated AZ91magnesium alloy using solutions containing neodymium, Corros. Sci. 173 (2020), 108741.
[33] J. Światowska, V. Lair, C. Pereira-Nabais, G. Cote, P. Marcus, A. Chagnes, XPS, XRD and SEM characterization of a thin ceria layer deposited onto graphite electrode for application in lithium-ion batteries, Appl. Surf. Sci. 257 (2011) 9110–9119.
[34] D.S. Wei, J.G. Wang, Y. Liu, D.W. Wang, S.Y. Li, H.Y. Wang, Controllable superhydrophobic surfaces with tunable adhesion on mg alloys by a simple etching method and its corrosion inhibition performance, Chem. Eng. J. 404 (2021), 126444.
[36] S.M. Ren, M.J. Cui, J.B. Pu, Q.J. Xue, L.P. Wang, Multilayer regulation of atomic boron nitride films to improve oxidation and corrosion resistance of cu, ACS Appl. Mater. Interfaces 9 (2017) 27152–27165.
[37] X. Liu, H.Q. He, T.C. Zhang, L. Ouyang, Y.X. Zhang, S.J. Yuan, Superhydrophobic and self-healing dual-function coatings based on mercaptabenzimidazole inhibitor-loaded magnesium silicate nanotubes for corrosion protection of AZ31B magnesium alloys, Chem. Eng. J. 404 (2021), 127106.
[38] I.A. Kartsonakis, A.C. Balaskas, E.P. Koumoulos, C.A. Charitidis, G. Kordas, ORMOSIL-epoxy coatings with ceramic containers for corrosion protection of magnesium alloys ZK10, Prog. Org. Coat. 76 (2013) 459–470.
[39] H. Yan, J.C, G. Wang, M. Cai, X. Wang, S.J. Song, X.Q. Fan, L. Zhang, H. Li, W. Li, M.H. Zhu, Towards long-term corrosion and wear protection of Al alloy: synergy of Ti3C2Tx flake and micro-arc oxidation coating, Corros. Sci. 174 (2020), 108813.
[40] S.V. Gnedenkov, S.L. Sinebryukhov, V.I. Sergienko, Electrochemical impedance simulation of a metal oxide heterostructure/electrolyte interface: a review, Russ. J. Electrochem. 42 (2006) 197–211.
[41] M.E. Orazem, N. Pébère, B. Tribollet, in: Enhanced Graphical Representation of Electrochemical Impedance Data, 2006, pp. 129–136.
[42] A. Jangde, S. Kumar, C. Blawert, Influence of glycerol on plasma electrolytic oxidation coatings evolution and on corrosion behaviour of coated AM50 magnesium alloy, Corros. Sci. 157 (2019) 220–246.
[43] Y. Zhang, C. Yan, F. Wang, W. Li, Electrochemical behavior of anodized Mg alloy AZ91D in chloride containing aqueous solution, Corros. Sci. 47 (2005) 2816–2831.
[44] L.M. Caladoa, M.G. Taryba, M.J. Carmezim, M.F. Montemor, Self-healing ceria-modified coating for corrosion protection of AZ31 magnesium alloy, Corros. Sci. 142 (2018) 12–21.
[45] L. Li, J. Gao, Y. Wang, Evaluation of cyto-toxicity and corrosion behavior of alkaliheat- treated magnesium in simulated body fluid, Surf. Coat. Technol. 185 (2004) 92–98.
[46] L. Lei, X. Wang, W. Liu, Q.W. Tang, Surface evaluation and electrochemical behavior of cerium conversion coating modified with silane on magnesium alloy, Surf. Interface Anal. 47 (2015) 466–473.

[47] F. Gong, J. Shen, R. Gao, X. Xie, X. Luo, Enhanced corrosion resistance of magnesium alloy by a silane-based solution treatment after an in-situ formation of the Mg(OH)2 layer, Appl. Surf. Sci. 365 (2016) 268–274.
[48] M. Mouanga, P. Berçot, J.Y. Rauch, Comparison of corrosion behaviour of zinc in NaCl and in NaOH solutions. Part I: corrosion layer characterization, Corros. Sci. 52 (2010) 3984–3992.
[49] T.F. Xiang, S.L. Zheng, M. Zhang, H.R. Sadig, C. Li, Bioinspired slippery zinc phosphate coating for sustainable corrosion protection, ACS Sustain. Chem. Eng. 6 (2018) 10960–10968.

Supporting information

A zinc-doped coating prepared on the magnesium alloy by plasma electrolytic oxidation for corrosion protection

Chao Yang[a], Hu Cai[a], Suihan Cui[a,*], Jian Huang[a], Jiayu Zhu[a], Zhongcan Wu[a], Zhengyong Ma[a], Ricky K. Y. Fu[b], Liyuan Sheng [c], Xiubo Tian[a], Paul K. Chu[b], Zhongzhen Wu[a,*]

[a] School of Advanced Materials, Peking University Shenzhen Graduate School, Shenzhen 518055, China

[b] Department of Physics, Department of Materials Science & Engineering, and Department of Biomedical Engineering, City University of Hong Kong, Tat Chee Avenue, Kowloon, Hong Kong, 999077, China

[c] PKU-HKUST ShenZhen-HongKong Institution, Shenzhen, 518057, China

* Corresponding author: cuish@pku.edu.cn (S.H. Cui) and wuzz@pkusz.edu.cn(Z.Z. Wu)

Table S1. The conductivity and pH value of the different electrolyte.

Samples	Electrolyte ($g \cdot L^{-1}$)			Conductivity ($ms \cdot cm^{-1}$)	pH
	$(NaPO_3)_6$	NaOH	$(CH_3COO)_2Zn$		
Passivated layer	20	3	—	14.52	12.71
Zn-0	20	—	—	5.70	6.09
Zn-5	20	—	5	7.15	5.38
Zn-10	20	—	10	8.34	5.49
Zn-15	20	—	15	9.36	5.61

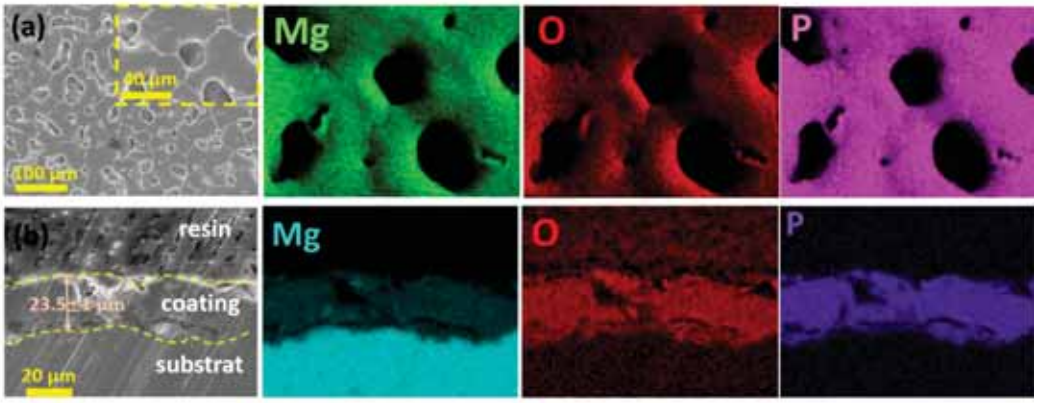

Fig. S1. The passivation dielectric layer prepared by first step of PEO: (a) Surface morphology and EDS analysis, (b) Cross-sectional morphology and EDS analysis.

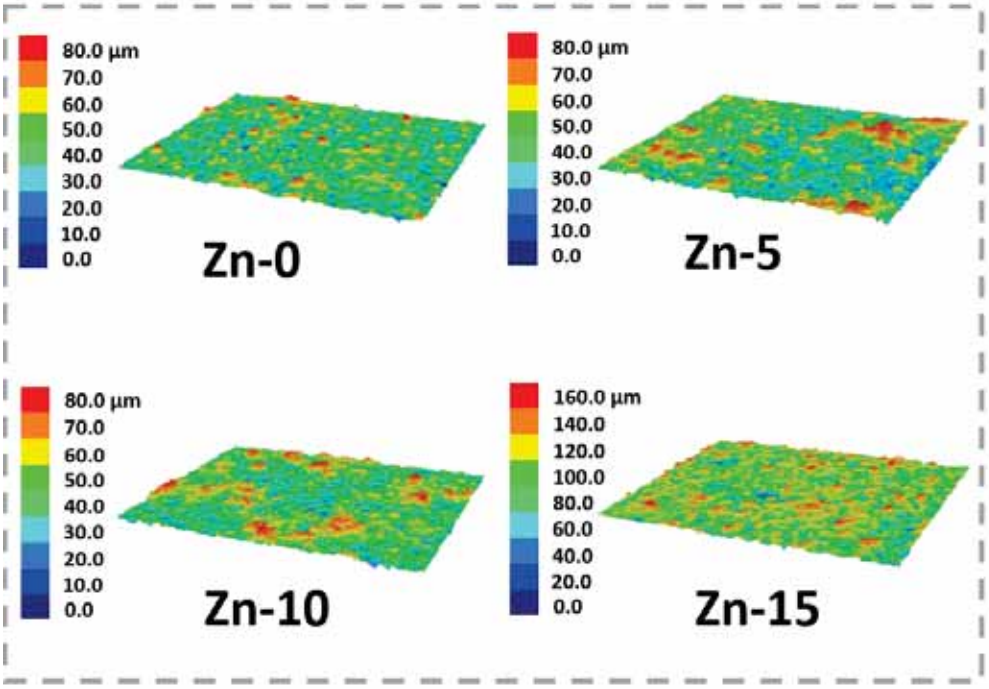

Fig. S2. CLSM images of the PEO coating prepared with different concentrations of Zn salt.

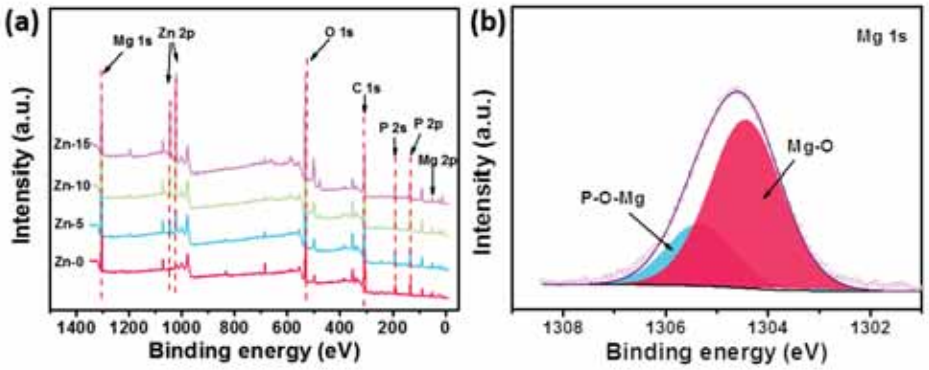

Fig. S3. XPS spectrum: (a) Total spectrum of the PEO coatings prepared with different concentrations of Zn salt, (b) Mg 1s spectrum of Zn-15.

Table S2. Different phase content of the coating prepared with different concentrations Zn.

Samples	Phase Content (%)		
	MgO	**$Mg_3(PO_4)_2$**	**$Zn_3(PO_4)_2$**
Zn-0	94.47	5.53	—
Zn-5	89.40	9.41	1.14
Zn-10	85.95	12.76	1.29
Zn-15	82.19	15.38	2.43

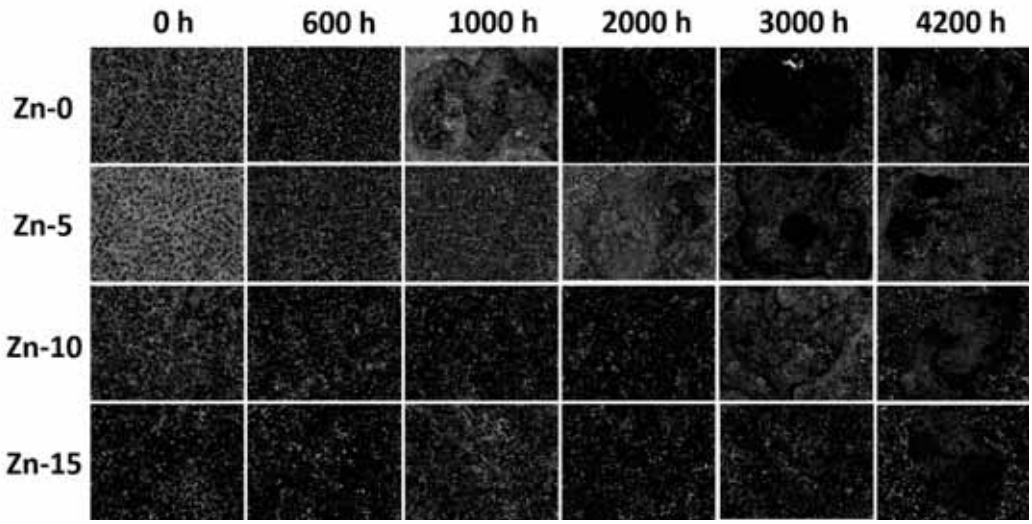

Fig. S4. CLSM images of the corroded PEO coatings with different Zn contents subjected to neutral salt spraying.

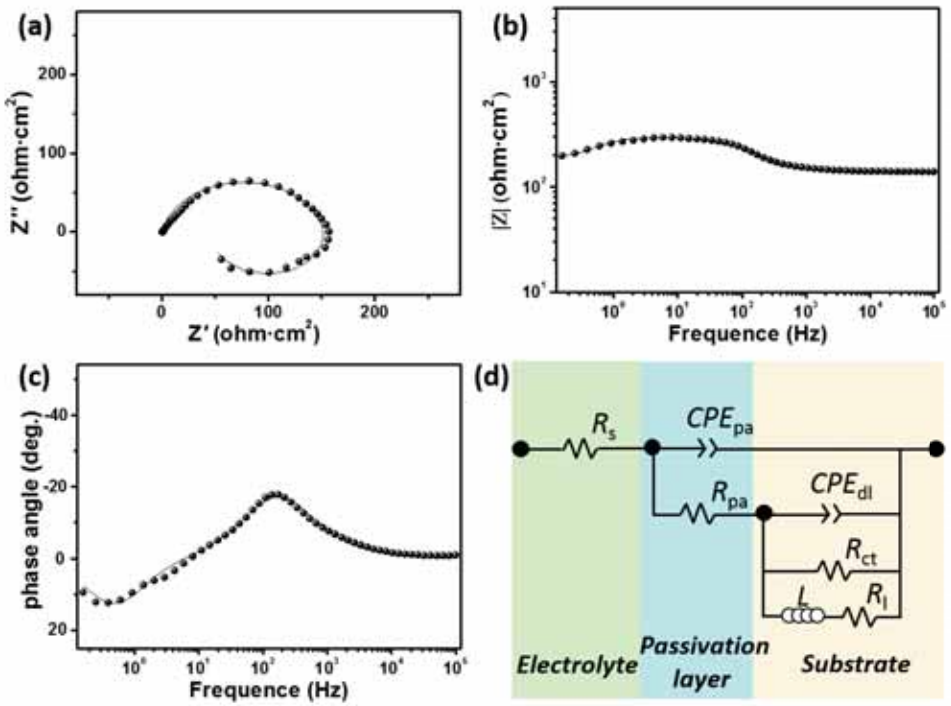

Fig. S5. EIS results of AZ31B: (a) Nyquist plot; (b) Bode impedance data; (c) Bode phase angle data; (d) Equivalent circuit.

Table S3. EIS results of AZ31B based on the equivalent circuit.

	AZ31B
$\mathbf{R_s\ (\Omega \cdot cm^2)}$	139.7
$\mathbf{CPE_{pa}\ (\Omega^{-1} \cdot cm^{-2} \cdot s^n)}$	8.082×10^{-6}
$\mathbf{n_{pa}}$	0.9347
$\mathbf{R_{pa}\ (\Omega \cdot cm^2)}$	41.42
$\mathbf{CPE_{dl}\ (\Omega^{-1} \cdot cm^{-2} \cdot s^n)}$	1.946×10^{-5}
$\mathbf{n_{dl}}$	0.8824
$\mathbf{R_{ct}\ (\Omega \cdot cm^2)}$	153.8
$\mathbf{L\ (H \cdot cm^2)}$	56.21
$\mathbf{R_l\ (\Omega \cdot cm^2)}$	66.21
χ	2.237×10^{-4}

Table S4. EIS result of Zn-0 after corrosion for different time based on the equivalent circuit.

Salt spraying time	0 h	600 h	1000 h	2000 h	3000 h	4200 h
R_s ($\Omega \cdot cm^2$)	142.3	129.8	180.2	172.6	159.4	164.5
CPE_d ($\Omega^{-1} \cdot cm^{-2} \cdot s^n$)	4.236×10^{-8}	—	—	—	—	—
n_d	0.9572	—	—	—	—	—
R_d ($\Omega \cdot cm^2$)	1.17×10^{3}	—	—	—	—	—
CPE_p ($\Omega^{-1} \cdot cm^{-2} \cdot s^n$)	2.496×10^{-6}	1.815×10^{-6}	6.543×10^{-6}	6.951×10^{-5}	9.144×10^{-5}	7.144×10^{-4}
n_p	0.787	0.525	0.9189	0.6572	0.2502	0.7034
R_p ($\Omega \cdot cm^2$)	3.583×10^{2}	1.686×10^{2}	7.724×10^{2}	0.648×10^{2}	0.473×10^{2}	0.299×10^{2}
CPE_{dl} ($\Omega^{-1} \cdot cm^{-2} \cdot s^n$)	5.437×10^{-6}	4.501×10^{-6}	1.614×10^{-6}	2.611×10^{-4}	1.798×10^{-3}	5.133×10^{-3}
n_{dl}	0.8887	1	0.4777	0.7163	0.7492	0.717
R_{ct} ($\Omega \cdot cm^2$)	3.368×10^{4}	1.551×10^{4}	3.847×10^{4}	2.858×10^{3}	1.210×10^{3}	2.570×10^{2}
L ($H \cdot cm^2$)	—	—	2.762×10^{3}	7.071×10^{3}	8.398×10^{3}	9.761×10^{3}
R_l ($\Omega \cdot cm^2$)	—	—	8.703×10^{3}	4.823×10^{3}	4.323×10^{3}	4.059×10^{3}
χ	5.6×10^{-4}	1.3×10^{-3}	7.7×10^{-3}	2.5×10^{-3}	5×10^{-5}	1.3×10^{-3}

Table S5. EIS results of Zn-5 after corrosion for different time based on the equivalent circuit.

Salt spraying time	0 h	600 h	1000 h	2000 h	3000 h	4200 h
R_s ($\Omega \cdot cm^2$)	140.6	146.6	160.1	137	186.2	229.1
CPE_d ($\Omega^{-1} \cdot cm^{-2} \cdot s^n$)	—	—	—	—	—	—
n_d	—	—	—	—	—	—
R_d ($\Omega \cdot cm^2$)	—	—	—	—	—	—
CPE_p ($\Omega^{-1} \cdot cm^{-2} \cdot s^n$)	2.564×10^{-6}	2.349×10^{-6}	6.543×10^{-6}	3.474×10^{-5}	5.939×10^{-5}	5.608×10^{-4}
n_p	0.6947	0.8967	0.9189	0.9285	0.6861	0.7482
R_p ($\Omega \cdot cm^2$)	9.345×10^{2}	8.652×10^{2}	7.724×10^{2}	6.230×10^{2}	3.940×10^{2}	1.084×10^{2}
CPE_{dl} ($\Omega^{-1} \cdot cm^{-2} \cdot s^n$)	6.752×10^{-7}	7.844×10^{-7}	1.614×10^{-6}	1.357×10^{-5}	1.565×10^{-4}	6.382×10^{-4}
n_{dl}	0.8809	0.9909	0.4777	0.709	1	0.8608
R_{ct} ($\Omega \cdot cm^2$)	9.697×10^{4}	6.995×10^{4}	3.847×10^{4}	9.142×10^{3}	5.889×10^{3}	3.408×10^{3}
L ($H \cdot cm^2$)	—	—	—	1.457×10^{3}	7.147×10^{3}	8.365×10^{3}
R_l ($\Omega \cdot cm^2$)	—	—	—	5.843×10^{3}	5.051×10^{3}	4.297×10^{3}
χ	4×10^{-3}	1×10^{-3}	7.7×10^{-3}	2×10^{-3}	3×10^{-3}	7×10^{-3}

Table S6 EIS results of Zn-10 after corrosion for different time based on the equivalent circuit.

Salt spraying time	0 h	600 h	1000 h	2000 h	3000 h	4200 h
R_s ($\Omega \cdot cm^2$)	208	199.9	203.5	179	191.8	163.2
CPE_d ($\Omega^{-1} \cdot cm^{-2} \cdot s^n$)	—	—	—	—	—	—
n_d	—	—	—	—	—	—
R_d ($\Omega \cdot cm^2$)	—	—	—	—	—	—
CPE_p ($\Omega^{-1} \cdot cm^{-2} \cdot s^n$)	1.510×10^{-7}	1.740×10^{-7}	1.548×10^{-6}	8.950×10^{-6}	2.649×10^{-5}	3.145×10^{-4}
n_p	0.7079	0.7995	0.8163	0.8529	0.7726	0.7356
R_p ($\Omega \cdot cm^2$)	2.041×10^{3}	1.536×10^{3}	1.260×10^{3}	8.929×10^{2}	5.427×10^{2}	2.345×10^{2}
CPE_{dl} ($\Omega^{-1} \cdot cm^{-2} \cdot s^n$)	2.155×10^{-7}	2.314×10^{-7}	3.804×10^{-7}	4.863×10^{-6}	1.024×10^{-5}	3.213×10^{-5}
n_{dl}	0.7593	1	0.9999	0.6526	0.9398	0.8403
R_{ct} ($\Omega \cdot cm^2$)	2.701×10^{5}	2.237×10^{5}	1.151×10^{5}	6.121×10^{4}	1.841×10^{4}	1.058×10^{4}
L ($H \cdot cm^2$)	—	—	—	—	1.058×10^{3}	3.691×10^{3}
R_l ($\Omega \cdot cm^2$)	—	—	—	—	4.466×10^{4}	6.938×10^{3}
χ	9×10^{-4}	3×10^{-3}	1.6×10^{-3}	1.1×10^{-3}	4×10^{-3}	2.4×10^{-4}

Table S7. EIS results of Zn-15 after corrosion for different time based on the equivalent circuit.

Salt spraying time	0 h	600 h	1000 h	2000 h	3000 h	4200 h
R_s ($\Omega \cdot cm^2$)	164.1	147.9	209.3	184.7	171.7	188.3
CPE_d ($\Omega^{-1} \cdot cm^{-2} \cdot s^n$)	7.452×10^{-8}	8.180×10^{-7}	—	—	—	—
n_d	0.9345	0.6577	—	—	—	—
R_d ($\Omega \cdot cm^2$)	2.73×10^{5}	3.167×10^{4}	—	—	—	—
CPE_p ($\Omega^{-1} \cdot cm^{-2} \cdot s^n$)	9.267×10^{-8}	1.245×10^{-7}	1.014×10^{-7}	3.542×10^{-6}	8.451×10^{-6}	7.355×10^{-5}
n_p	0.6637	0.9581	0.7948	0.8414	0.8709	0.9331
R_p ($\Omega \cdot cm^2$)	5.783×10^{4}	3.876×10^{4}	1.306×10^{4}	5.115×10^{3}	3.824×10^{3}	1.990×10^{3}
CPE_{dl} ($\Omega^{-1} \cdot cm^{-2} \cdot s^n$)	7.456×10^{-8}	7.372×10^{-8}	1.585×10^{-7}	2.410×10^{-7}	1.352×10^{-6}	4.403×10^{-6}
n_{dl}	0.9344	0.8589	0.833	0.8692	0.5247	0.7918
R_{ct} ($\Omega \cdot cm^2$)	3.788×10^{5}	3.242×10^{5}	2.915×10^{5}	1.826×10^{5}	8.920×10^{4}	2.530×10^{4}
L ($H \cdot cm^2$)	—	—	—	—	—	2.678×10^{3}
R_l ($\Omega \cdot cm^2$)	—	—	—	—	—	7.403×10^{4}
χ	2×10^{-3}	2.2×10^{-3}	2.6×10^{-3}	1.7×10^{-4}	7×10^{-4}	1.5×10^{-3}

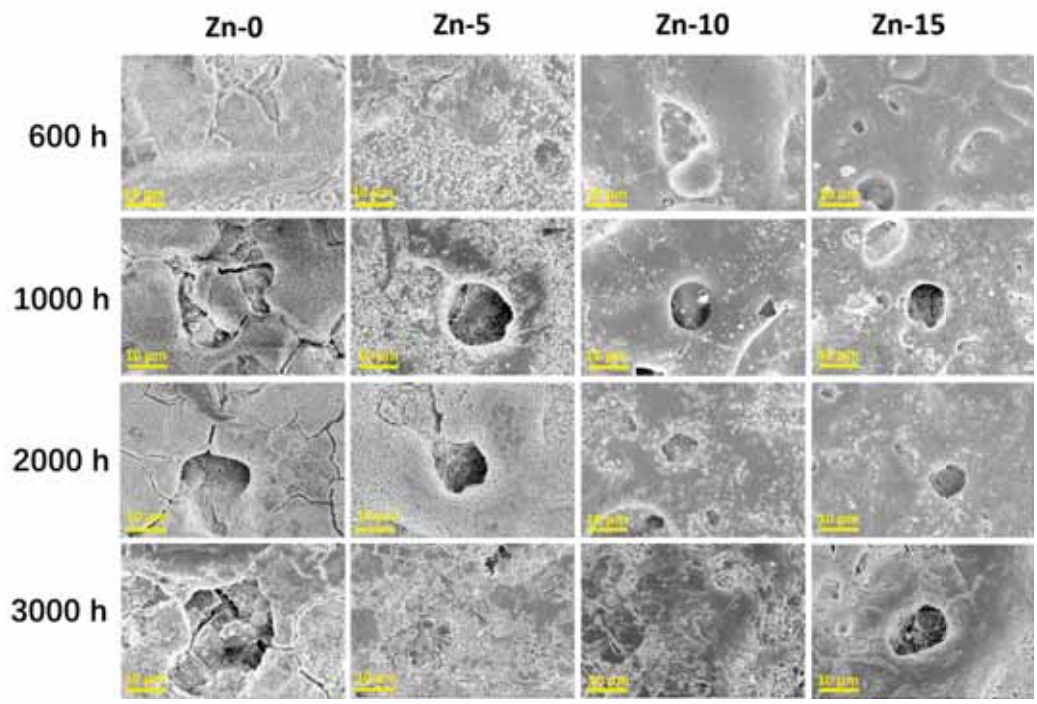

Fig. S6. Corroded PEO coatings with different Zn contents after neutral salt spraying.

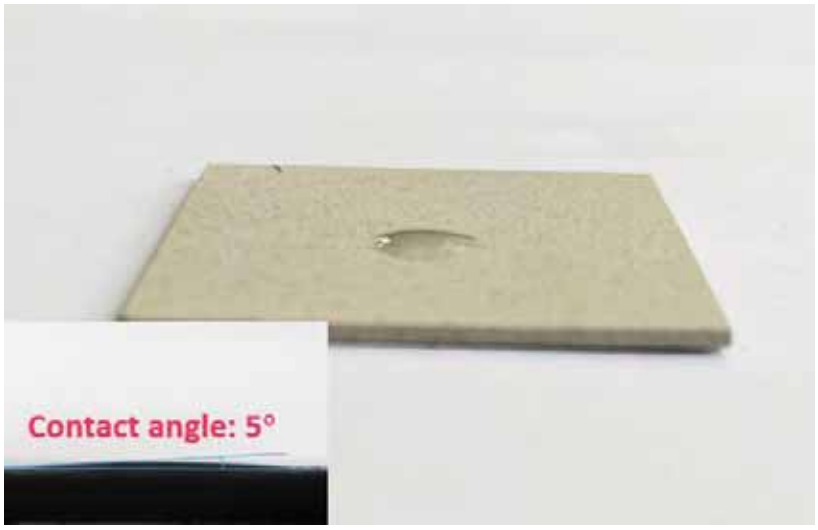

Fig. S7. Salt solution droplet on the Zn-15 coating.

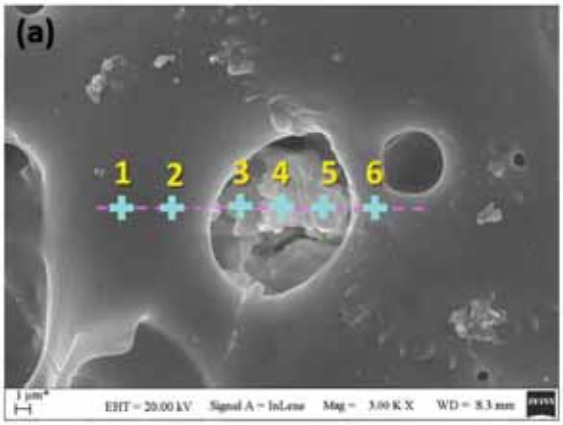

(b)

Region	Atomic ratio of Elements (%)				
	C	O	Mg	P	Zn
1	13.82	59.54	14.08	10.91	1.65
2	12.84	54.18	16.12	14.69	2.17
3	18.33	40.63	13.28	13.98	13.78
4	20.10	40.37	11.14	12.21	16.18
5	17.65	44.61	11.74	13.24	12.76
6	17.94	51.32	13.30	13.72	3.72

Fig. S8. EDS results obtained from different regions on Zn-15 before corrosion: (a) Tested regions and (b) Elemental concentrations measured from the selected areas.

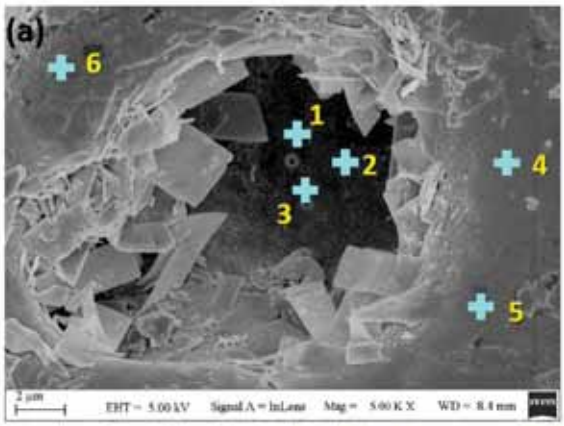

(b)

Region	Atomic ratio of Elements (%)				
	C	O	Mg	P	Zn
1	25.41	32.42	6.93	15.80	19.44
2	16.82	29.11	8.39	17.64	28.04
3	14.43	28.42	8.85	24.74	23.56
4	19.66	49.08	15.64	13.79	1.83
5	17.55	56.71	12.97	10.80	1.97
6	21.02	53.60	12.49	10.91	1.98

Fig. S9. EDS results obtained from different regions on Zn-15 after corrosion: (a) Tested regions and (b) Elemental concentrations measured from the selected areas.